TECHNISCHE UNIVERSITÄT WIEN

ILSB Institute of Lightweight Design and Structural Biomechanics

Institutsbericht 312

Linear continuum modeling of lattice materials by means of the Finite Element Method

M.M. Schasching[1], M. Todt[1]

1 Institute of Lightweight Design and Structural Biomechanics,
TU Wien, Gumpendorfer Straße 7, A-1060 Vienna, Austria

Wien, 12. Oktober 2021

INSTITUTE OF LIGHTWEIGHT DESIGN AND STRUCTURAL BIOMECHANICS
Gumpendorfer Straße 7/BE02/E317, A-1060 Vienna, Austria
Tel: +43 1 58801/31701, Fax: +43 1 58801/31799
e-Mail: sec@ilsb.tuwien.ac.at, http://www.ilsb.tuwien.ac.at

Contents

Notation

Throughout this report italic and boldface letters are referred to scalar and tensorial quantities, respectively, whereas underlined lowercase and a single tilde placed below uppercase letters designate tensors of first and second order, respectively. Furthermore, square brackets indicate tensorial quantities with respect to a Cartesian basis resulting in vectors or matrices. Quantities with respect to the microscopic and macroscopic level are denoted by lower- and upper-case letters, respectively. All other quantities are referred to within the corresponding passage. Einstein's summation convention is applied everywhere unless stated otherwise.

Scalar notation

a, b	...	scalars

Tensor notation

$\underline{\mathbf{a}}$, $\underline{\mathbf{b}}$	...	vectors
$\underset{\sim}{\mathbf{A}}$, $\underset{\sim}{\mathbf{B}}$	...	second–order tensors
$\underset{\approx}{\mathbb{A}}$, $\underset{\approx}{\mathbb{B}}$	...	fourth–order tensors

Index notation

a_i, b_i	...	vectors using index notation
A_{ij}, B_{ij}	...	second–order tensors using index notation
$\mathbb{A}_{ijkl}$, $\mathbb{B}_{ijkl}$	...	fourth–orders tensor using index notation

Tensor notation with respect to Cartesian basis

$[\underline{\mathbf{a}}]$, $[\underline{\mathbf{b}}]$	...	vectors or first–order tensors
$[\underset{\sim}{\mathbf{A}}]$, $[\underset{\sim}{\mathbf{B}}]$	...	second–order tensors
$[\underset{\approx}{\mathbb{A}}]$, $[\underset{\approx}{\mathbb{A}}]$	...	fourth–order tensors

Matrix notation (component ordering see Appendix A)

$[\underset{\sim}{\mathbf{A}}]$, $[\underset{\sim}{\mathbf{B}}]$	...	second–order tensors using matrix notation
$[\underset{\approx}{\mathbb{A}}]$, $[\underset{\approx}{\mathbb{B}}]$	...	fourth–order tensors using matrix notation

Symbols

A_{bc}	...	Area of base cell	in m^2
$\underset{\approx}{\mathbb{A}}$	...	Fourth-order elasticity tensor	in $\mathrm{N/mm}^2$
$\underset{\approx}{\mathbb{B}}$	...	Fourth-order elasticity tensor	in N
$\underset{\approx}{\mathbb{C}}$	...	Fourth-order elasticity tensor	in N/mm
$[\underset{\sim}{\mathbb{D}}]$	...	Elasticity tensor in matrix notation	in -
ϵ_{ijk}	...	Third-order LEVI-CHIVITA permutation tensor in index notation	in -
$\underset{\sim}{\boldsymbol{\varepsilon}}$	...	Non-symmetric linearized strain tensor	in -
$[\underline{\boldsymbol{\varepsilon}}]$	...	Linearized vector of strain components in matrix notation	in -
E_{s}	...	Young's modulus solid material	in $\mathrm{N/mm}^2$
$\underline{\mathbf{f}}$	...	Body force density vector	in N/kg
$\underline{\mathbf{g}}$	...	Body moment density vector	in Nmm/kg
G_{s}	...	Shear modulus solid material	in $\mathrm{N/mm}^2$
$\underset{\sim}{\boldsymbol{\kappa}}$	...	Linearized curvature tensor	in 1/mm
L	...	Length at macroscale	in mm
l	...	Length at microscale	in mm
$\underset{\sim}{\mathbf{m}}$	...	Couple stress tensor	in N/mm
MxM	...	Number of elements	in -
NxN	...	Number of base cells	in -
ν_{s}	...	Poisson's ratio solid material	in -
$\underline{\boldsymbol{\phi}}$	...	Microrotation vector	in rad
ψ	...	Strain energy density functional	in $\mathrm{N/mm}^2$
ρ	...	Density	in $\mathrm{kg/m}^3$
$\underset{\sim}{\boldsymbol{\sigma}}$	...	Non-symmetric stress tensor	in $\mathrm{N/mm}^2$
$[\underline{\boldsymbol{\sigma}}]$	...	Vector of stress components in matrix notation	in $\mathrm{N/mm}^2$
$\underline{\mathbf{u}}$	...	Displacement vector	in mm
$\underline{\mathbf{U}}$	...	Nodal displacement-rotation vector	in mm*or*rad
W	...	Strain energy	in Nm

Symbols for Operation

$\det[\underset{\sim}{\mathbf{A}}]$	...	Determinant of a matrix
$[\underset{\sim}{\mathbf{A}}]^{\mathrm{T}}$	...	Transpose of a matrix

The Levi-Chivita symbol, i.e., the permutation tensor, is defined as

$$\epsilon_{ijk} = \begin{cases} 1 & i,j,k = 1,2,3;\ 2,3,1;\ 3,1,2 \\ -1 & i,j,k = 3,2,1;\ 1,3,2;\ 2,1,3 \\ 0 & i = j,\ i = k,\ j = k \end{cases}$$

1 Introduction

Lattice structures are gaining importance in a wide range of biomedical and engineering applications, such as aircraft panels in modern aircrafts. The underlying internal architecture, or microstructure, is acting as a main contributor to the mechanical properties of such materials [3]. On the basis of this knowledge and progressing additive manufacturing techniques, the opportunity of designing man-tailored structures comes up to meet desired properties. Lattice structures show a high strength-to-density ratio and, consequently, are of special interest in lightweight design. Further weight savings can be achieved by manufacturing very slender lattice structures. Utilization of components made of such materials goes hand in hand with the necessity of appropriate descriptive models in order to achieve reliability concerning safety reasons. In the current report, finite-sized lattice structures are investigated to consider boundary- and size effects.

Slender lattice structures are prone to structural instabilities when exposed to compressive stress states, which may be caused by both tensile and compressive overall loading conditions. The compressive strength of these materials is governed by the buckling load rather than the strength of the parent material [17]. If the buckling load is exceeded, buckling modes will show wavelengths of different magnitudes depending on various parameters such as, boundary conditions, free edges, localization of deformation [16] etc.. In the following, local and global instabilities are referred to buckling modes with wavelength of the same order as the microscale and macroscale, respectively. The primary focus of the descriptive model is set on local instabilities as a first step for the sake of simplicity. The basis for the investigations will be numerical simulations of the structural response by means of the Finite Element Method (FEM).

Discrete models of lattice materials, i.e., resolving each lattice member by finite elements explicitly, may be the first choice for investigating the structural response of such materi-

als implying the drawback of time consuming pre-processing. Moreover, as the model size increases, FEM simulations may exhibit high computational effort, especially, when considering the aforementioned buckling nonlinearity.

In order to address the computational efficiency, one may appreciate to treat the underlying internal architecture as an effective material instead of resolving the discrete structure. An appropriate constitutive law on the basis of such a discrete structure may serve as a basis to account for the underlying periodic microstructure and allow to capture local instabilities arising from certain loading conditions. Common constitutive laws are based on a strain energy functional derived via various homogenization techniques exploiting different continuum theories. Models accounting for stretching-dominated, or pin-jointed, periodic networks are addressed, e.g., in [20] and [10], [9], [21] using standard and second-gradient continuum theories, respectively.

These models may not be suited best to describe the behavior of bending-dominated structures, i.e., slender rigid-jointed networks, as the deformation of its members is characterized by joint displacements as well as rotations as independent fields. Consequently, the modeling of lattice materials in terms of continuum theory ask for higher order theories capable of accounting for both fields. In a first step, the micropolar field theory may serve as the basis for an appropriate descriptive model [19]. The mechanical foundation of micropolar continua was mainly developed by Eringen and his co-workers based on the ideas of the Cosserat brothers [8] and is summarized within the book of Eringen [13]. Therein, also an overview of the historical background of micropolar continuum theory can be found.

To capture local instabilities in lattice materials caused by certain loading conditions large displacements and finite rotations as well as finite strains have to be considered. Herein, finite strains are related to the effective response of the lattice structure and are governed by large displacements or finite rotations of the underlying microstructure rather than to material nonlinearities of the parent material.

In a first step, to challenge the complexity of the involved nonlinearities in micropolar continua, a descriptive model capable of the structural response in the linear regime is sought for. The model developed in [15] is used, which exploits the proposed homogenization approach for lattice materials with periodic microstructure developed in [7], and was further implemented as an user element `UEL` in the commercial FEM software `ABAQUS`. The homogenization approach provides two different sets of micropolar elastic constants depending on the assumptions made. The two sets differ in both sign and a constant value, and affect only the micropolar constants that link the couple stresses and curvatures. Some shortcomings on the predictive capabilities of the model have already been reported in [25]. It was examined that the model is not capable of accurately capturing size effects, i.e., the dependence of the effective material properties on the sample size, but at least showing similar tendency as the corresponding discrete model.

The aim of the current report is to further investigate the predictive capabilities and limitations of the micropolar continuum element suggested by [15]. For this purpose, the structural response of square lattices in the linear regime is investigated by means of the FEM. A comparison between the micropolar continuum and discrete models is performed, where the latter serve as reference. The models are subjected to adequate loading conditions to represent simple shear and bending load cases. Particular emphasize is placed on the study of structural response in terms of the two sets of derived micropolar constants.

Section 2 focuses on the required linear micropolar field theory, whereas Section 3 gives an overview of the homogenization approach as given in [15] being based on [7]. The numerical simulations performed are presented in Section 4. Finally, Section 5 concludes the current report and gives an outlook for further research on this topic.

2 Linear Micropolar Continuum

The micropolar theory belongs to the class of higher order theories, where the displacement degrees of freedom (DOF) (also referred to as CAUCHY or sometimes BOLTZMANN type DOFs) are supplemented by independent rotational DOFs. A rigid triad, described by its basis vectors $\underline{\mathbf{D}}_i$ and $\underline{\mathbf{d}}_i$ in the reference and material configuration, respectively, is attached to each material point $\mathcal{P}$ of the continuum body $\mathcal{B}$ and accounts for the independent rotation field, see Figure 1. All further considerations are restricted to a Cartesian basis with corresponding basis vectors $\underline{\mathbf{e}}_i$ for $i = 1, 2, 3$ within the Euclidean space $\mathcal{E}$.

The following equations describing the micropolar field theory are used for the development of the user element and are taken from [13], considering only static problems, where no temperature fields are involved. No differentiation between Eulerian and Lagrangian description has to be made as all further considerations are restricted to linear theory.

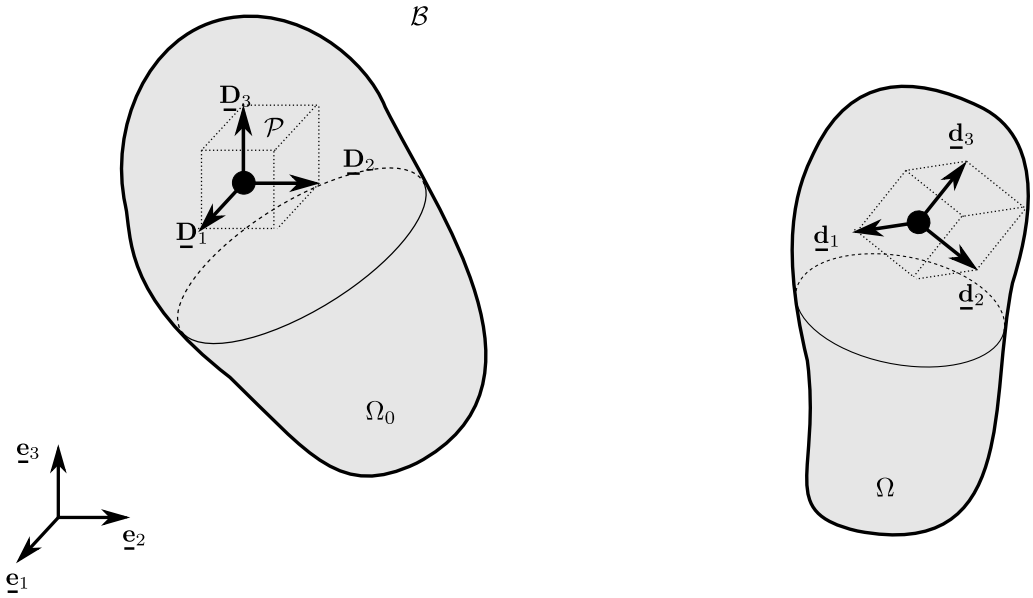

Figure 1: Micropolar continuum in reference (domain Ω_0) and material (domain Ω) configuration.

The balance laws are given by

$$\begin{aligned} \sigma_{ji,j} + \rho f_i &= 0 \\ m_{ji,j} + \epsilon_{imn}\sigma_{mn} + \rho g_i &= 0 \end{aligned} \tag{1}$$

corresponding to the balance of linear momentum and balance of moment of momentum, respectively. Thereby, σ_{ji} denotes the non-symmetric stress tensor, ρ the density, f_i the body force density, m_{ji} the couple stress tensor, ϵ_{ijk} the third-order LEVI-CHIVITA permutation tensor and g_i the body moment density. The definition of the LEVI-CHIVITA permutation tensor is given on page 4. It is worth mentioning, that the stress tensor in a CAUCHY continuum, in contrast, is symmetric, i.e., $\sigma_{ji} = \sigma_{ij}$.

The linearized strain measure follows as

$$\begin{aligned} \varepsilon_{ji} &= u_{i,j} + \epsilon_{ijk}\phi_k \\ \kappa_{ji} &= \phi_{i,j} \end{aligned} \tag{2}$$

where ε_{ji} is the strain tensor, u_i the displacement vector, ϕ_i the microrotation (or also called microdisplacement) vector, and κ_{ji} the curvature tensor. Both, strain and curvature tensor are non-symmetric in general [2].

The strain energy density functional (or strain energy potential) of a micropolar continuum for the nonthermal case can be given as

$$\begin{aligned} \psi(\varepsilon_{ij}, \kappa_{ij}) &= \frac{1}{2}(\mathbb{A}_{klmn}\varepsilon_{kl}\varepsilon_{mn} + \mathbb{B}_{klmn}\kappa_{kl}\kappa_{mn} + 2\mathbb{C}_{klmn}\varepsilon_{kl}\kappa_{mn}) \\ &= \frac{1}{2}(\sigma_{ij}\varepsilon_{ij} + m_{ij}\kappa_{ij}) \end{aligned} \tag{3}$$

with $\mathbb{A}_{klmn}, \mathbb{B}_{klmn}, \mathbb{C}_{klmn}$ as fourth-order elasticity tensors.

As all further considerations are restricted to conservative systems, stresses and couple stresses can be derived directly from the strain energy potential by

$$\begin{aligned} \sigma_{ij} &= \frac{\partial \psi}{\partial \varepsilon_{ij}} \\ m_{ij} &= \frac{\partial \psi}{\partial \kappa_{ij}} \end{aligned} \tag{4}$$

as well as the elasticity tensors can be given as

$$\begin{aligned} \mathbb{A}_{ijkl} &= \frac{\partial^2 \psi}{\partial \varepsilon_{ij} \partial \varepsilon_{kl}} \\ \mathbb{B}_{ijkl} &= \frac{\partial^2 \psi}{\partial \kappa_{ij} \partial \kappa_{kl}} \\ \mathbb{C}_{ijkl} &= \frac{\partial^2 \psi}{\partial \varepsilon_{ij} \partial \kappa_{kl}} \end{aligned} \tag{5}$$

The constitutive law can then be given as

$$\begin{aligned} \sigma_{ji} &= \mathbb{A}_{jikl} \varepsilon_{kl} + \mathbb{C}_{jikl} \kappa_{kl} \\ m_{ji} &= \mathbb{C}_{klij} \varepsilon_{kl} + \mathbb{B}_{ijkl} \kappa_{kl} \end{aligned} \tag{6}$$

For centrosymmetric lattices the elasticity tensor $\mathbb{C}_{jikl}$ vanishes, which is the case for the uniform periodically repeating two-dimensional (2D) base cells discussed in [15] and [24]. This holds also true for isotropic materials [13].

The constitutive law in a compact matrix-vector notation for centrosymmetric lattices and isotropic materials follows as

$$\begin{bmatrix} [\underset{\sim}{\boldsymbol{\sigma}}] \\ [\underline{\mathbf{m}}] \end{bmatrix} = \underbrace{\begin{bmatrix} [\underset{\sim}{\mathbb{A}}] & [\underset{\sim}{\mathbf{0}}] \\ [\underset{\sim}{\mathbf{0}}]^{\mathrm{T}} & [\underset{\sim}{\mathbb{B}}] \end{bmatrix}}_{[\underset{\sim}{\mathbb{D}}]} \begin{bmatrix} [\underline{\boldsymbol{\varepsilon}}] \\ [\underline{\boldsymbol{\kappa}}] \end{bmatrix} \tag{7}$$

with $[\underset{\sim}{\mathbb{D}}]$ as the corresponding micropolar elasticity matrix.

In the current report, only two-dimensional problems are considered, where the dimension of the out-of-plane direction $\underline{\mathbf{e}}_3$ is much larger than those of the two remaining in-plane directions $\underline{\mathbf{e}}_1$ and $\underline{\mathbf{e}}_2$. Therefore, plane strain assumptions are used as an acceptable approximation. All physical quantities are independent of x_3 and, hence, just depending on x_1, x_2 and t. The constitutive law in matrix-vector notation considering centrosymmetric lattices in two dimensions as given in [15] leads to

$$\underbrace{\begin{bmatrix} \sigma_{11} \\ \sigma_{22} \\ \sigma_{12} \\ \sigma_{21} \\ m_{13} \\ m_{23} \end{bmatrix}}_{[\underline{\boldsymbol{\sigma}}]} = \underbrace{\begin{bmatrix} D_{11}(=\mathbb{A}_{1111}) & D_{12} & & & & \\ D_{12} & D_{22} & & & & \\ & & D_{33} & D_{34} & & \\ & & D_{34} & D_{44} & & \\ & & & & D_{55} & \\ & & & & & D_{66} \end{bmatrix}}_{[\underset{\sim}{\mathbb{D}}]} \underbrace{\begin{bmatrix} u_{1,1} \\ u_{2,2} \\ u_{2,1} - \phi \\ u_{1,2} + \phi \\ \phi_{,1}(=\kappa_{13}) \\ \phi_{,2}(=\kappa_{23}) \end{bmatrix}}_{[\underline{\boldsymbol{\varepsilon}}]} \tag{8}$$

where $\phi = \phi_3$ as the only remaining microrotation.

3 Effective Material Properties

In [15] linear elastic micropolar material constants of various periodic lattice structures such as, square, triangle, diamond etc., are derived via an energy approach based on [7]. Thereby, an appropriate base cell of the discrete lattice is identified and its strain energy is constructed by the strain energy contributions of its individual members. The strain energy of each lattice member can be expressed as a function of its joint displacements $\underline{\mathbf{u}}_I, \underline{\mathbf{u}}_J$ and rotations ϕ_I, ϕ_J as

$$W^{IJ}(\underline{\mathbf{u}}_I, \underline{\mathbf{u}}_J, \phi_I, \phi_J) \tag{9}$$

where I and J denote the joints at both ends.

The joint displacements and rotations of each member are then expressed in terms of a commonly shared origin joint O located in the center of the base cell. The kinematics at the origin O are denoted by $\underline{\mathbf{u}}$ and ϕ. A Taylor series expansion of the kinematics of each remaining joint K of the lattice is then developed, where only terms up to the second order are retained, and can be given as

$$\begin{aligned} \underline{\mathbf{u}}_K &\approx \underline{\mathbf{u}} + l_{OK}\frac{\partial \underline{\mathbf{u}}}{\partial t_{OK}} + \frac{1}{2}l_{OK}^2\frac{\partial^2 \underline{\mathbf{u}}}{\partial t_{OK}^2} \\ \phi_K &\approx \phi + l_{OK}\frac{\partial \phi}{\partial t_{OK}} + \frac{1}{2}l_{OK}^2\frac{\partial^2 \phi}{\partial t_{OK}^2} \end{aligned} \tag{10}$$

with t_{OK} and l_{OK} as the spatial orientation and length of the member, respectively.

The strain energy density of the continuum approximation is then constructed by summing the strain energies of each member i and referring the sum to the area of the base cell A_{bc}. It can be given as

$$\psi = \frac{1}{A_{\mathrm{bc}}}\left(\sum_{i=1}^{n} W_i^{OK}(\underline{\mathbf{u}}_K, \phi_K)\right) \tag{11}$$

where n is the number of lattice members involved. Inserting the displacement and rotation fields of Eq. (10) into (11) and performing several algebraic transformations using the equations given in [15] give the strain energy density of the continuum approximation in terms of strains ε_{ij} and curvatures κ_{ij} as $\psi(\varepsilon_{ij}, \kappa_{ij})$, where the stresses and the components of the elasticity tensors can be determined via Eq. (4) and (5), respectively.

The derived components of the elasticity matrix $[\underset{\sim}{\mathbb{D}}]$ depend on the geometry of the underlying lattice structure and on the isotropic material properties of its members, further referred to as solid material. Furthermore, the components D_{55} and D_{66} are negative or positive values depending on retaining or ignoring second order derivatives in the Taylor series expansion of the displacement and rotation field, respectively, see Eq. (10). For further details on the derivation of the material constants, it is referred to [7] and [15].

The scope of the current report is restricted to the investigation of square lattices. The elasticity matrix $[\underset{\sim}{\mathbb{D}}]$ for such lattices is given as

$$[\underset{\sim}{\mathbb{D}}] = \begin{bmatrix} \frac{E_1 l_1}{l_2} & & & & & \\ & \frac{E_2 l_2}{l_1} & & & & \\ & & \frac{12k_1}{l_1 l_2} & & & \\ & & & \frac{12k_2}{l_1 l_2} & & \\ & & & & \underbrace{-\frac{2k_1 l_1}{l_2}\left(\text{or } \frac{4k_1 l_1}{l_2}\right)}_{D_{55}^{neg} \text{ (or } D_{55}^{pos})} & \\ & & & & & \underbrace{-\frac{2k_2 l_2}{l_1}\left(\text{or } \frac{4k_2 l_2}{l_1}\right)}_{D_{66}^{neg} \text{ (or } D_{66}^{pos})} \end{bmatrix}. \tag{12}$$

The quantities are composed of $E_i = \dfrac{Et}{l_i}$, $k_i = \dfrac{Et^3}{12 l_i}$ with $i = 1, 2$ and

$$E = \frac{E_\mathrm{s}}{(1-\nu_\mathrm{s}^2)}, \tag{13}$$

where E_s and ν_s denote the Young's modulus and the Poisson ratio of the solid material, respectively. The cell wall thickness t is assumed to be constant and the length of each beam l in i-direction results in $l = l_1 = l_2$ for square lattices. The out-of-plane thickness with respect to the plane strain assumption is defined as $h = 1$.

It is worth mentioning, that if one assumes a constant ratio t/l while keeping the marcoscopic domain constant, then the elasticity components $D_{11}, D_{22}, D_{33}, D_{44}$ will be independent of the number of base cells comprising the lattice, in contrast, to D_{55} and D_{66}. The latter will vanish for decreasing base cell sizes while keeping the macroscopic domain constant in size, i.e., $\lim_{l\to 0} D_{ii} = 0$ for $i = 5, 6$. In general, the CAUCHY continuum will be preserved, if the couple stresses and the body moments vanish [2].

4 Finite Element Analyses

4.1 Implementation as an ABAQUS User Element

A displacement- and rotation-based two-dimensional quadrilateral finite element was implemented within the framework of the commercial FEM software ABAQUS as an user element based on [15]. The element is capable of accounting for the independent fields of displacement and rotation which are necessary for the field equations of 2D linear micropolar continua. Both fields as well as the geometry of the element are discretized using the same linear interpolation functions. The resulting 2D isoparametric finite element considers plane strain assumptions and will further be called CPE4MP. A full Gaussian quadrature scheme is exploited to integrate the inherent quantities of the element over its domain. Furthermore, internal body forces and moments can be considered as distributed loads and are accessible via the ABAQUS keyword *DLOAD.

The governing field equations and the material constants with respect to the square lattice of the developed CPE4MP have already been reported in Section 2 and 3, respectively. The resulting element stiffness matrix and corresponding interpolation functions can be found in Appendix A.

4.1.1 Verification of CPE4MP Implementation - Patch Test

A patch of incompatible (or nonconforming) elements may not lead to monotonically convergent solutions under mesh refinement, but if it passes the so-called *patch test* developed for displacement-based elements by [14] at least non-monotonic convergence will be ensured [4]. The *patch test* is said to be passed, i.e., the patch of elements satisfies the *completeness of an element assemblage* [4], if the patch of elements exhibits a constant strain state

under certain boundary conditions and reproduces exact results which are obtained by a corresponding analytical solution.

As the *patch test* is used to assess incompatible finite element meshes, properly formulated displacement-based elements making up compatible meshes will automatically pass it. Hence, it offers the possibility of assessing the correct implementation of newly developed finite elements, if it is properly extended to the requirements of the specific element type to be tested. An proper extension to account for two-dimensional linear elastic micropolar elements is proposed by [22]. Therein, the authors suggest three tests in total to be satisfied to address all equilibrium states of constant strain possible within two-dimensional linear elastic micropolar theory.

The patch of elements, as depicted in Figure 2, satisfies *Test 1* and *Test 2* when it is capable of reproducing equilibrium states of constant strains with $\varepsilon_{12} = \varepsilon_{21}$ and $\varepsilon_{12} \neq \varepsilon_{21}$, respectively. *Test 3* assesses the ability of recovering constant states of curvature. The corresponding boundary conditions, loadings and the analytical solutions of each test are taken from [22] and are given in Table 1 with some corrections made as a consequence of some inconsistencies, which will be explained in the next paragraph. The equations for the displacements and the rotation for each test serve as boundary conditions applied on the outer nodes $5-8$, and serve as the analytical solution for the inner nodes $1-4$. Internal body forces p_i and moments q are applied on every element.

A slight inconsistency could be noticed within the equations for *Test 2* and *Test 3* in [22] regarding the value of the constant α chosen therein. To obtain consistent values for both tests the arrangement of parentheses concerning the equations in Table 1 had to be changed, see details in Appendix C.

The developed user element `CPE4MP` passes the *patch test* independent of the underlying material, as expected. The results obtained by the simulation and the corresponding analytical

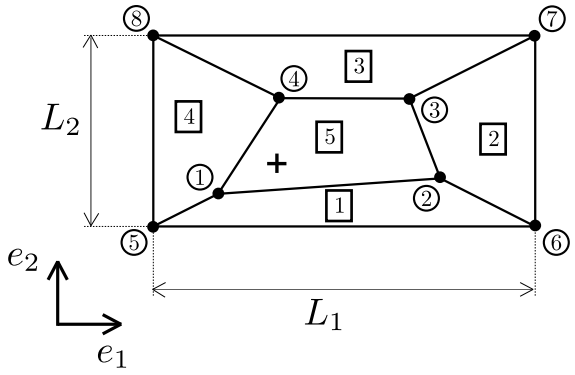

Figure 2: Element assemblage of the *patch test* with cross indicating integration point 1 of element 5.

(exact) solution considering isotropic material behavior are given in Table 3. The isotropic micropolar material constants used for the simulations are taken from [22] and are converted in order to obtain equivalent material constants corresponding to the definition given in [13], see Table 2. The two-dimensional elasticity matrix for a micropolar isotropic material on the basis of Eq. (8) can then be given as

Table 1: *Patch test* - Boundary conditions, loadings and polynomial solutions taken from [22] including corrected arrangement of parentheses.

Test 1
$u_1 = 10^{-3}(x_1 + (1/2)x_2), \quad u_2 = 10^{-3}(x_1 + x_2), \quad \phi = 10^{-3}(1/4), \quad p_1 = p_2 = q = 0$
$\Rightarrow \sigma_{11} = \sigma_{22} = 4, \quad \sigma_{12} = \sigma_{21} = 1.5, \quad m_1 = m_2 = 0$
Test 2
$u_1 = 10^{-3}(x_1 + (1/2)x_2), \quad u_2 = 10^{-3}(x_1 + x_2), \quad \phi = 10^{-3}((1/4) + 1/(4\alpha)), \quad p_1 = p_2 = 0, \quad q = 1$
$\Rightarrow \sigma_{11} = \sigma_{22} = 4, \quad \sigma_{12} = 1, \quad \sigma_{21} = 2, \quad m_1 = m_2 = 0$
Test 3
$u_1 = 10^{-3}(x_1 + (1/2)x_2), \quad u_2 = 10^{-3}(x_1 + x_2), \quad \phi = 10^{-3}((1/4) + 1/(2\alpha)(x_1 - x_2)),$
$p_1 = p_2 = 1, \quad q = 2(x_1 - x_2)$
$\Rightarrow \sigma_{11} = \sigma_{22} = 4, \quad \sigma_{12} = 1.5 - (x_1 - x_2), \quad \sigma_{21} = 1.5 + (x_1 - x_2), \quad m_1 = -m_2 = 2l^2/\alpha$

Table 2: Isotropic micropolar material parameters.

Definition used in [22]	Definition used in [13]
$G = 1000, v = 0.25, l = 0.1, \alpha = 0.5$	$\lambda = 1000, \kappa = 1000, \gamma = 40, \mu_c = 500$

$$[\underset{\sim}{\mathbb{D}}_{\text{MPiso}}] = \begin{bmatrix} \lambda + 2\mu & \lambda & & & & \\ \lambda & \lambda + 2\mu & & & & \\ & & \mu_c + \kappa & \mu_c & & \\ & & \mu_c & \mu_c + \kappa & & \\ & & & & \gamma & \\ & & & & & \gamma \end{bmatrix} \tag{14}$$

The used `CPE4MP` implementation is quite similar to the one suggested in [22]. Therein, the element accuracy is further investigated on the basis of a more realistic engineering problem, namely, a stress concentration problem, i.e., a notched plate under tension. The results of all the different element types developed in [22] are in good agreement with the corresponding known analytical ones, except for the results for the linearly interpolated triangular element. Consequently, it is assumed that it is dispensable to check the element accuracy in the current report.

Table 3: *Test 3* - Nodal displacements at node 2 and stresses at integration point 1 of element 5.

	$U_1 \cdot 10^{-3}$	$U_2 \cdot 10^{-3}$	$\phi \cdot 10^{-3}$	σ_{11}	σ_{22}	σ_{12}	σ_{21}	$m_1 = -m_2$
`CPE4MP`	0.1950	0.2100	0.4000	4.0000	4.0000	1.4590	1.5410	0.0400
Exact	0.1950	0.2100	0.4000	4.0000	4.0000	1.4590	1.5410	0.0400

4.2 Numerical Investigations

The main focus of the current report is set on the investigation of the capabilities and limitations of the implemented finite element `CPE4MP` describing the response of a corresponding discrete lattice in the linear regime. For this purpose, adequate problems are sought for to be able to compare continuum and discrete solutions. If the separation of scale is not satisfied, i.e., the length scale of the microstructure and of the overall structure size are of the same magnitude, a proper choice with respect to the load case is to be made. Otherwise, local effects will dominate the overall response of the model, as e.g., comparing indentation load cases. This will even be more pronounced, if the characteristic base cell size, l, of the lattice meets the size of the elements used for discretizing the continuum.

A simple shear load case is used to address the comparability of discrete and continuum model, and additionally, to invoke the rotation field, see Figure 3 left. As a second assessment, a lattice beam under bending is employed in order to investigate the predictive capabilities of the continuum model considering a more realistic engineering problem, see Figure 3 right. The maximum displacements U_1 and U_2 are 0.2 mm and 20 mm for the shear and bending load case, respectively.

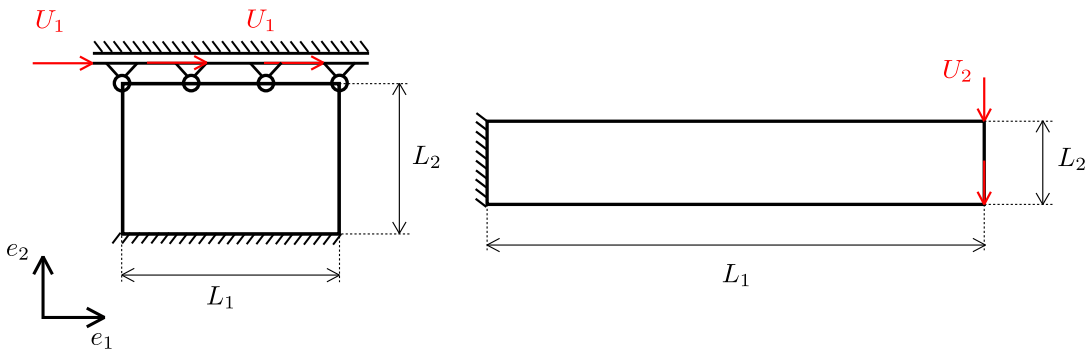

Figure 3: Simple shear (left) and bending (right) load case.

The influence of the number of base cells comprising a lattice may alter the overall structural response in a severe way, especially if the base cell size increases compared to the global size of the structure, as is known as size effect. The size effect of repetitive lattices mainly depends on the topology of the free surfaces which is determined by the geometry of the base cell. In the case of a square lattice, `L` or `+` shaped base cells will lead to a free-surface showing a *closed-* or *open-boundary*, respectively. Therefore, two different discrete lattice models serve as references for the continuum model to address this issue and will further be called *closed-* (or `L`) and *open-boundary* (or `+`) discrete models.

Besides, it is to remark that `ABAQUS` does not offer any possibility to directly contour-plot simulation results obtained by analyses involving user elements [1]. Therefore, the post-processing is conducted via `Python` programming language exploiting the package `matplotlib` to overcome these shortcomings.

4.2.1 Lattice under Simple Shear

To assess the length scale behavior of the model, the influence of the number of base cells forming the lattice on the strain energy is investigated where for the respective continuum models the lattice is discretized using various sets of MxM continuum elements. In other words, the influence of the number of base cells NxN within the number of continuum elements MxM on the strain energy is studied with $\mathrm{N}, \mathrm{M} \in \mathbb{N}^{+}$. For the sake of brevity, this will further be called **NxN in MxM** and is schematically illustrated in Figure 4. As the length scale behavior of the model has already been partly examined in [25], special emphasize is set on investigating the rotation field. Additionally, the influence on the structural response of both positive and negative derived elasticity matrix components is studied, referred to as D_{55}^{pos} and D_{66}^{pos} as well as D_{55}^{neg} and D_{66}^{neg}, respectively.

In Table 4 the global size of the lattice is determined by L_1 and L_2 describing the overall quadrilateral domain of the mesh and representing the macro-scale, whereas the size of the

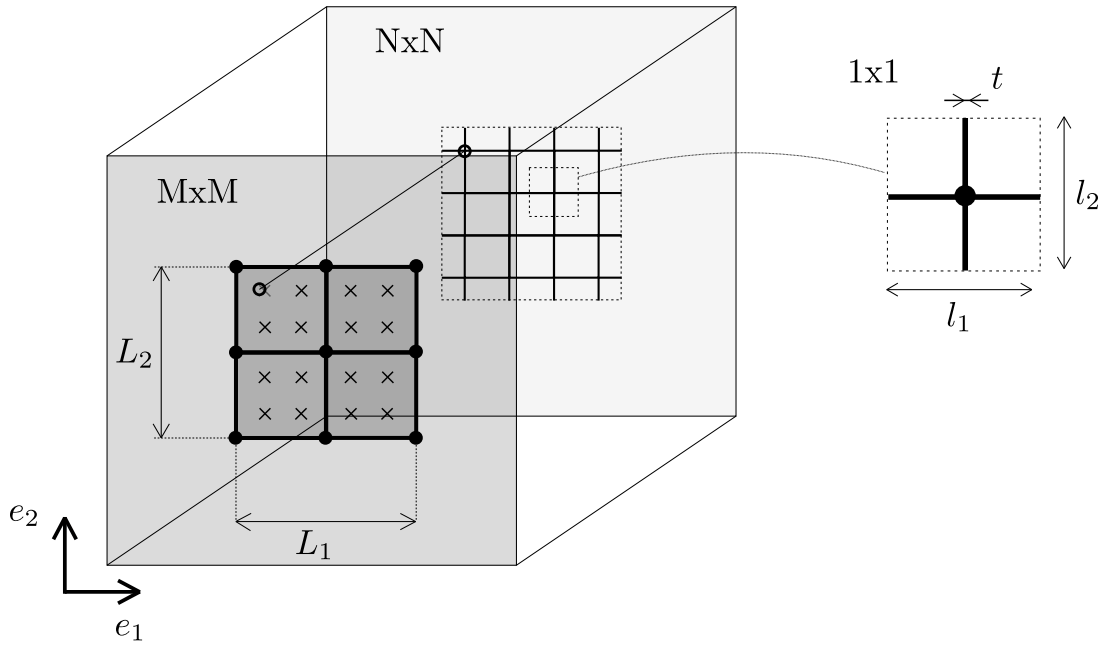

Figure 4: Schematic illustration of discretized domain by MxM finite elements representing NxN base cells comprising a lattice. Integration points and intersection points are indicated by x- and ∘-markers, respectively.

Table 4: Geometrical dimensions and material properties regarding the simple shear load case.

L_1 in mm	L_2 in mm	h in mm	E_s in MPa	ν_s (/)	l_1 in mm	l_2 in mm	t in mm	NxN (/)
1.0	1.0	1.0	120000.0	0.3	0.25	0.25	0.0125	4x4
1.0	1.0	1.0	120000.0	0.3	0.125	0.125	0.00625	8x8
1.0	1.0	1.0	120000.0	0.3	0.0625	0.0625	0.003125	16x16

underlying lattice, i.e., the geometry of the rectangular base cell, is determined by the cell wall lengths l_1, l_2 as well as the thickness t, see Figure 4. In the following, the characteristic length of the underlying square lattice is determined by $l = l_1 = l_2$. Furthermore, the isotropic solid material properties of the lattice members, namely, the Young's modulus and the Poisson ratio are referred to as E_s and ν_s, respectively.

The discrete lattice models are discretized by planar, linear TIMOSHENKO beam elements. Thereby, each cell wall of a single base cell is discretized by 6 elements resulting in 12 elements per base cell. This discretization allows the deformation state to be adequately captured as studies on mesh refinements had shown beforehand. The material and geometrical properties for the discrete models are given in Table 4, with the shear modulus of the isotropic solid material $G_s = \dfrac{E_\mathrm{s}}{2 \cdot (1 + \nu_\mathrm{s})}$, the cross-section $A_\square = t \cdot h$ and the geometrical moment of inertia $I_\square = \dfrac{t^3 \cdot h}{12}$. To account for plane strain assumptions, the Young's modulus E_s and the shear modulus G_s are converted according to Eq. (13).

Both discrete models show the same volume of solid material and, therefore, the elements on the outer boundary of the *closed-boundary* model are assigned half of the cross-section and geometrical moment of inertia, resulting in $A_\square/2$ and $I_\square/2$, respectively.

Strain energy

Strain energies of *closed-* and *open-boundary* discrete lattice models for a various number of base cells NxN are compared to those of their corresponding continuum counterparts considering mesh refinement MxM for positive and negative material constants in Figures 5a and 5b, respectively. The number of base cells NxN comprising the discrete models are varied using 4x4, 8x8 and 16x16, while keeping the volume of the inherent solid material constant and preserving the dimensions of the macroscopic domain as given in Table 4. Hence, resulting in 9.75% of the whole volume to be occupied by the solid material, which of course, is also true for the underlying lattice within the continuum models.

The strain energy of the continuum model, which considers positive material constants, clearly shows a monotonic convergence behavior under mesh refinement MxM at increasing NxN, cf. Figure 5a. In contrast, the strain energy of the continuum model, which considers negative material constants, seems to show some kind of oscillatory convergence behavior under mesh refinement, cf. Figure 5b. In order to clarify, if the solution shows a divergence or at least a non-monotonic convergence behavior, further investigations need to be done by increasing the number of base cells involved. Consequently, the following discussion on the strain energy focuses only on the micropolar continuum model with positive material constants.

The micropolar continuum model shows good agreement with the discrete models, if the discretization MxM is properly chosen with respect to the base cells involved. The *closed-* and *open-boundary* discrete models can be considered as upper and lower bound for the continuum model, respectively. It is worth noting, that the strain energies of the *closed-* and *open-boundary* discrete models show a clear convergence towards a common value with an increasing number of base cells involved as the so-called size effect decreases. For quantitative evidence on the capability of the model to capture size effects it is referred to [25]. Force-

displacement diagrams of discrete and continuum counterparts for lattices comprising 4x4 and 16x16 base cells can be found in the Appendix B, cf. Figure 17.

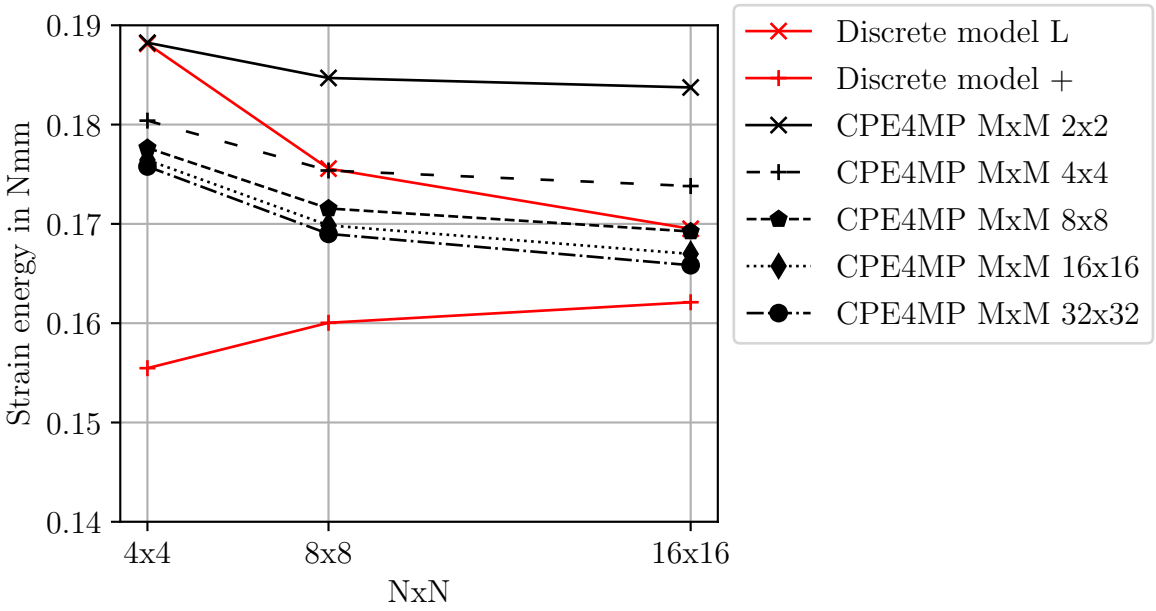

(a) D_{55}^{pos} and D_{66}^{pos}

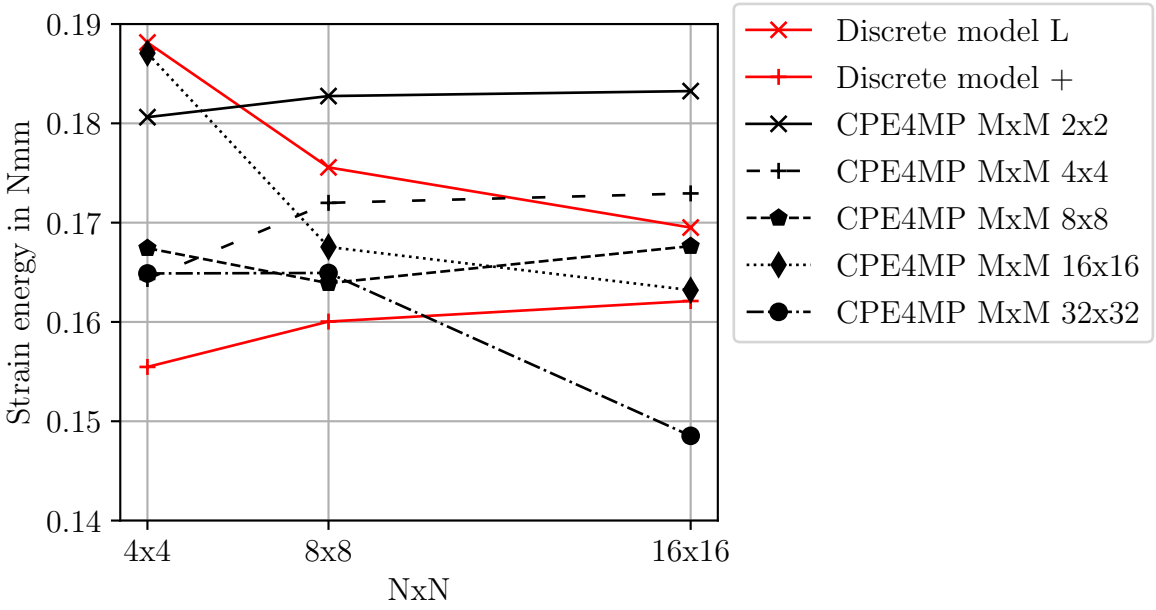

(b) D_{55}^{neg} and D_{66}^{neg}

Figure 5: Comparison of strain energies of *closed-* and *open-boundary* discrete lattice models for various NxN and corresponding continuum counterparts considering D_{55}^{pos} and D_{66}^{pos} as well as D_{55}^{neg} and D_{66}^{neg} under mesh refinement MxM for (a) and (b), respectively

Rotation field

The rotation fields obtained for the continuum model for different mesh-sizes representing a discrete lattice comprised of 4x4 base cells are shown for positive and negative material constants in Figures 6 and 7, respectively. The continuum model with positive constants clearly shows convergence behavior of the rotation field under mesh refinement. The resulting pattern shows continuously decreasing rotations from the bottom to a quarter of the height and levels off to a constant value, cf. Figure 6. If the element size meets the characteristic length of the underlying lattice, the rotation field is already completely resolved. In contrast, the rotation field of the continuum model with negative material constants shows such a behavior only, when the element size is equal to or larger as the characteristic length of the underlying lattice, cf. Figure 7. For element sizes below the characteristic length, l, the rotation field shows some kind of wave-like patterns, cf. Figure 7b and 7d. The wave-like patterns miss out a clear interpretation of the behavior of the rotation field when compared to the discrete model. The absence of a contour plot of the latter impedes a clear comparison between continuum and discrete models.

Therefore, a quantitative comparison of the rotation field between discrete and continuum model is performed. For this purpose, the rotations around the x_3-axis are evaluated along the second column of the physical lattice located at $x_1 = 0.375$, cf. Figure 8. The rotations of the discrete model are directly available via nodal output values as the nodes coincide with the geometry of the physical lattice. These are evaluated at the intersection points and the corresponding vertical lattice members connected to these points, cf. Figure 4. To evaluate the rotations of the continuum model the location of each intersection point is to be mapped onto the domain of the continuum model. The location of intersection points does usually not coincide with the nodes of the finite element mesh. Therefore, interpolation of the nodal values on the basis of the element shape functions is used in order to evaluate the rotation at

the location of interest. An visual explanatory of mapping the physical intersection points onto the continuum model is indicated by the ∘-marker in Figure 4.

The continuum model with positive constants shows converging rotations over the height towards the discrete solution under mesh refinement, cf. Figure 8a - 8c. Contrary, the model with negative constants shows an oscillating behavior with respect to the rotations under mesh refinement, cf. Figure 8d - 8f. The rotations at the intersection points of the lattice for continuum and discrete model show very good agreement in the far-field of the bearing point, except if negative material constants are used in combination with element sizes below the characteristic length, l, cf. 8f. In the vicinity of the bearing point, the high gradients with respect to the intersection points can only be resolved if element sizes below the characteristic length, l, in combination with positive material constants are used. Furthermore, the continuum model is not capable of capturing local gradients in the rotation field indicated by the garland like line representing the rotations within the individual lattice members in Figure 4, independent of the sign of the material constants D_{55} and D_{66}. Higher order field theory, i.e., micromorphic continuum theory, in conjunction with an appropriate derivation of material constants would be necessary to account for these local rotational gradients.

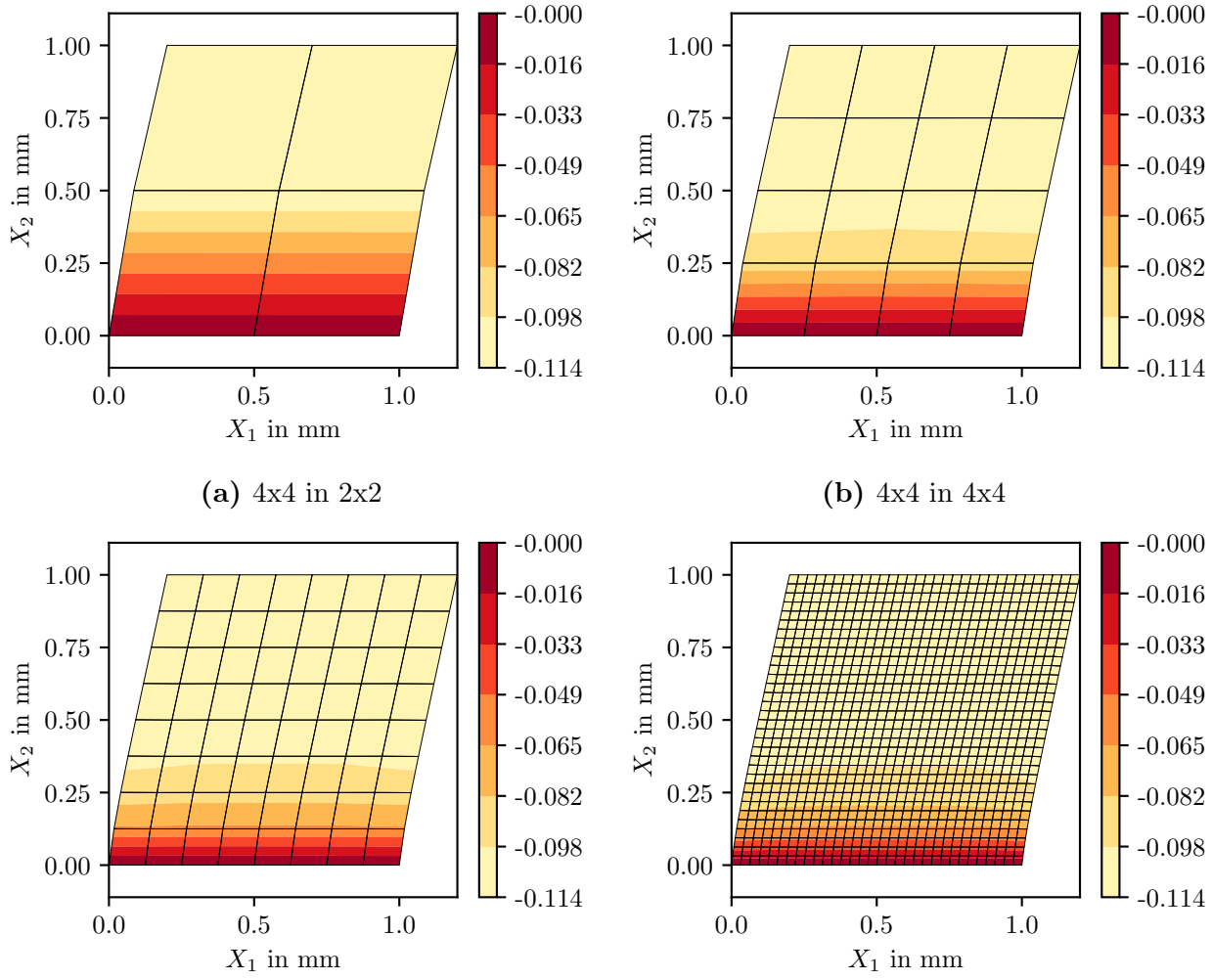

(a) 4x4 in 2x2

(b) 4x4 in 4x4

(c) 4x4 in 8x8

(d) 4x4 in 32x32

Figure 6: Rotation fields of the continuum model with D_{55}^{pos} and D_{66}^{pos} for various discretization MxM representing a 4x4 discrete lattice.

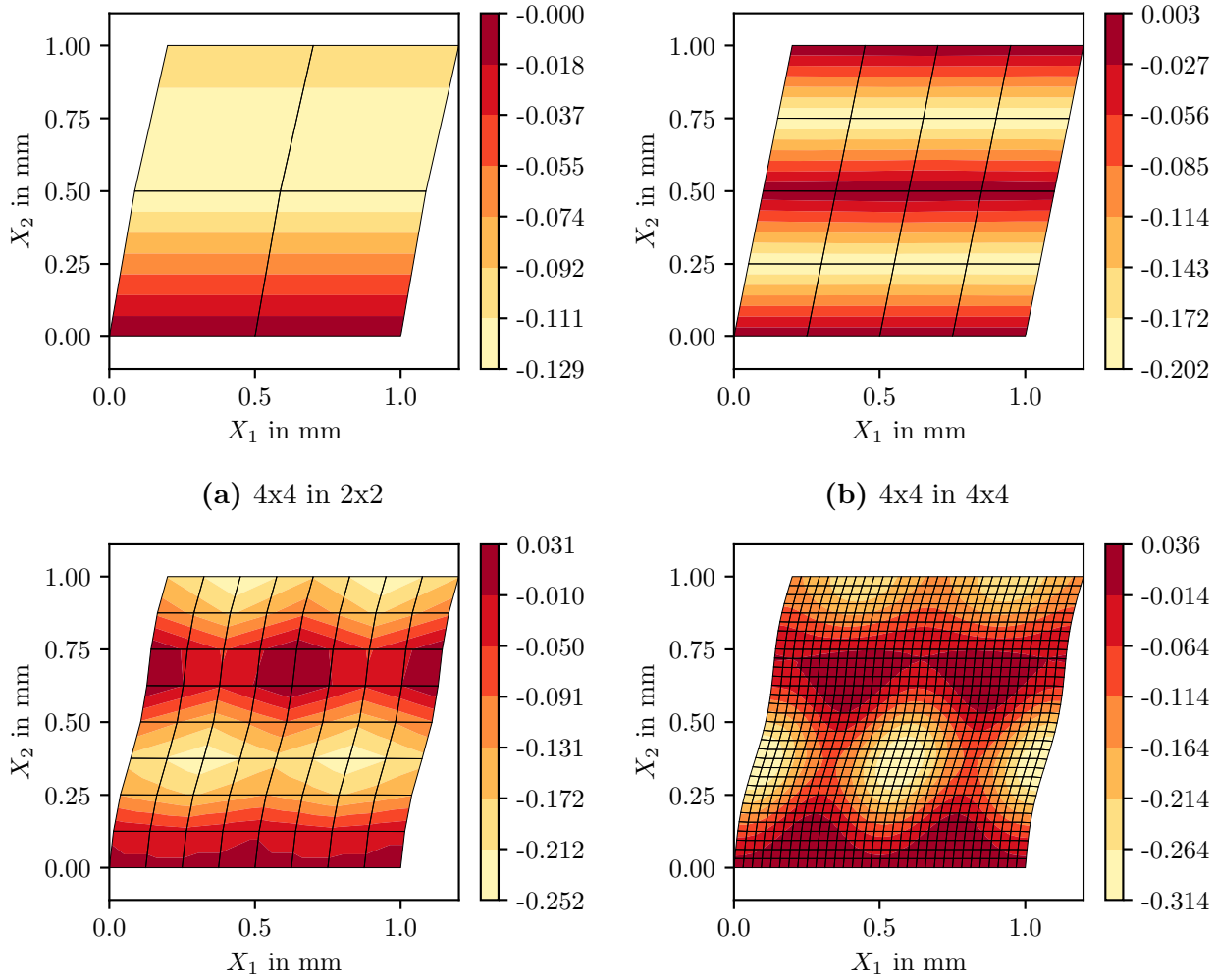

(a) 4x4 in 2x2

(b) 4x4 in 4x4

(c) 4x4 in 8x8

(d) 4x4 in 32x32

Figure 7: Rotation fields of the continuum model with D_{55}^{neg} and D_{66}^{neg} for various discretization MxM representing a 4x4 discrete lattice.

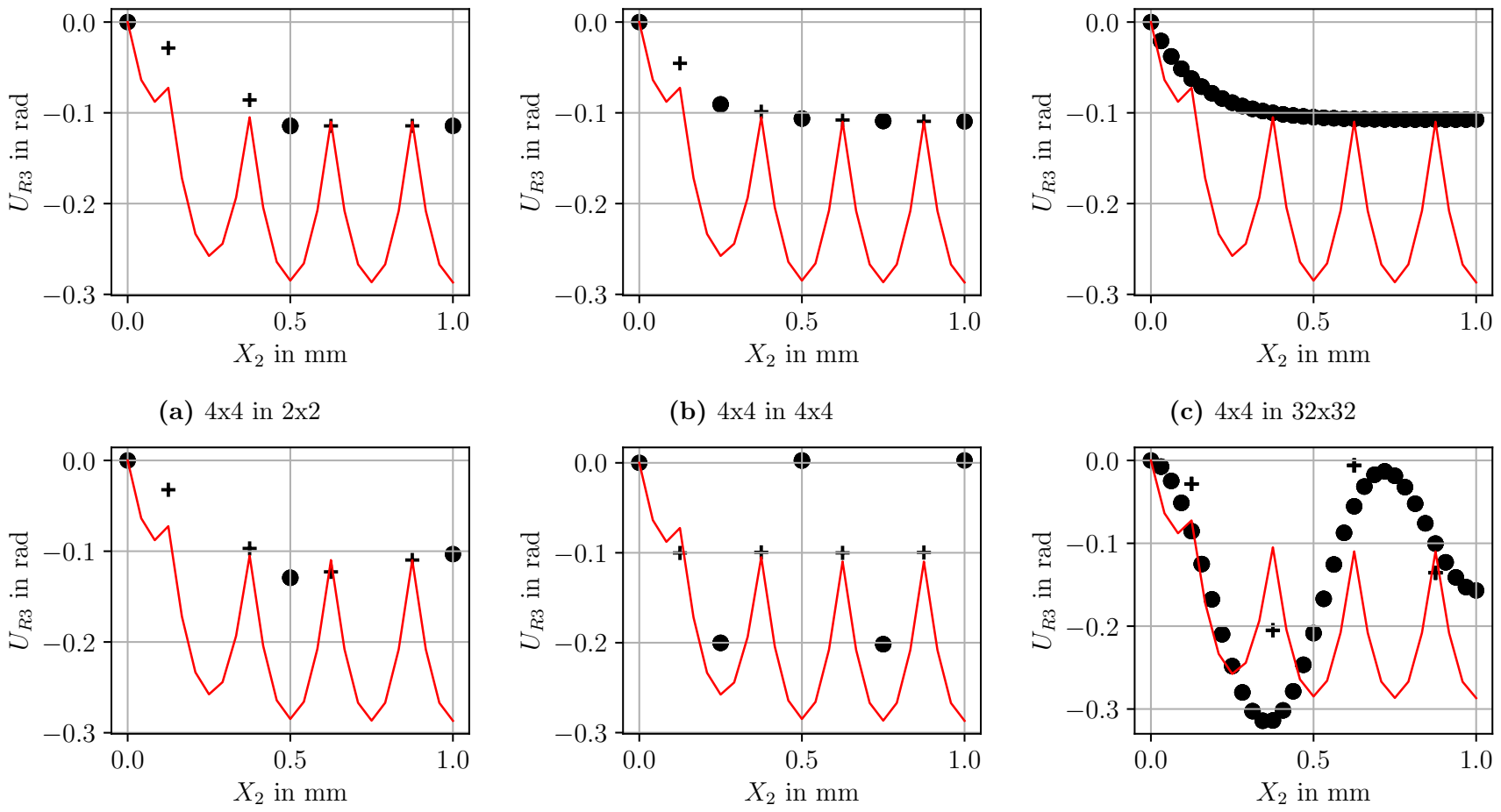

(a) 4x4 in 2x2 **(b)** 4x4 in 4x4 **(c)** 4x4 in 32x32

(d) 4x4 in 2x2 **(e)** 4x4 in 4x4 **(f)** 4x4 in 32x32

Figure 8: Rotational DOF ϕ of discrete model along the 2-direction at $x_1 = 0.375$ indicated by the solid line and of continuum model with positive and negative D_{55} and D_{66} for (a) - (c) and (d) - (f), respectively, indicated by the markers. The markers + and • correspond to intersection nodes of the lattice at $x_1 = 0.375$ and to nodes at $x_1 = 0.375 + l_1/2$, respectively.

Reduced integration

The model possesses an inherent length scale, namely, the characteristic length, l. The question may arise if there exists a relationship between the number of integration points (IPs) and the number of base cells involved within a single element. An hypothesis to be proofed could be formulated as follows: "A single integration point represents a single base cell and, therefore, similar patterns in the rotation field are expected to show up for the same total number of integration points within the model". More precisely, a comparison between models comprising MxM and (Mx2)x(Mx2) contiunuum elements to discretize the domain using full and reduced integration, respectively, is sought for, which results the same total number of integration points for both models. The influence of the total number of integration points on the resulting rotation field is investigated only considering negative material constants, since with positive constants the effect will not be reasonably pronounced.

The basis for comparison is a lattice comprising 4x4 base cells. The domain is discretized by 2x2, 16x16 and 32x32 elements using full integration, which results in 4x4, 32x32, and 64x64 integration points, respectively. In the case of reduced integration, the domain is discretized by 4x4, 32x32 and 64x64 elements, which results in 4x4, 32x32, and 64x64 integration points, respectively. The models considering 4x4 integration points show a different rotation field and indicate that there is no clear relationship between a single integration point and a single base cell, see Figures 9a and 9b. This seems also to be the case, using a finer discretization of the domain resulting in 32x32 integration points as indicated by Figures 9c and 9d. The absolute values of the rotation fields do not show good agreement, however, both fields appear to show a similar wave-like pattern. They show a kind of phase shift in vertical and horizontal direction while preserving the corresponding wavelengths. If 64x64 integration points are considered, both fields show the same wave-like pattern but different absolute values. Hence, the fields resulting from full and reduced integration converge towards the same wave-like pattern when the same total number of integration points are considered.

For a further comparison, all rotation fields available for the case of full integration depicted in Figure 7 can be found for the reduced integration in the Appendix B, cf. Figure 18.

Evolution of the wave-like pattern under mesh refinement

The rotation field shows convergence behavior under mesh refinement if positive material constants are used. This seems not to be the case if negative material constants are used. In this case, the question arises, if the rotation field converges towards a specific wave-like pattern under mesh refinement when a certain discretization of the domain is reached as indicated by Figure 7 and 9. Therefore, further investigations on the basis of a lattice comprising 8x8 base cells are conducted using various levels of discretization and full integration.

The rotation field evolves into a specific field of wave-like pattern under mesh refinement as shown in Figure 10. The pattern shows a phase shift in vertical and horizontal direction while preserving the corresponding wavelengths. This behavior has already been observed for the lattice comprinsing 4x4 base cells, cf. Figure 7c and 7d. If the discretization is M $\approx 2L/l$ the pattern becomes visible and gets more pronounced for finer meshes, i.e., M $> 2L/l$. The wavelength in horizontal direction for both lattices seems twice the characteristic length l. In vertical direction, the wavelength is approximately about three times the characteristic length l. Note that although the pattern converges qualitatively, the values of rotations seems to diverge quantitatively.

This wave-like patterns may correspond to structural instabilities within the lattice. Further investigations of this connection is beyond the scope of the current report.

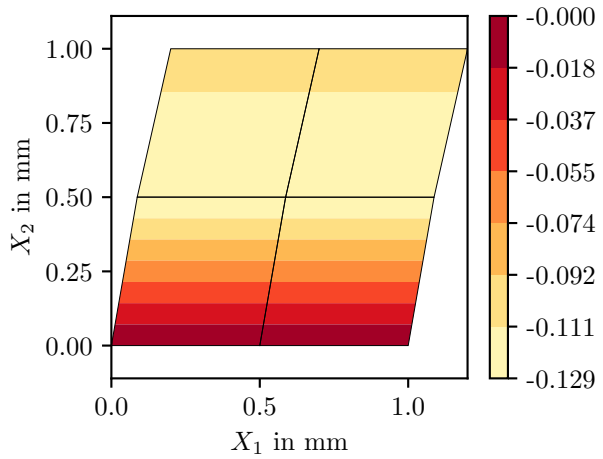

(a) 4x4 in 2x2 fully integrated 4x4 IPs

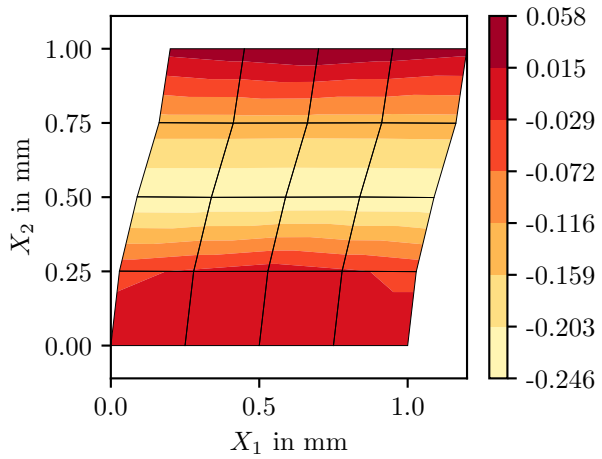

(b) 4x4 in 4x4 reduced integrated 4x4 IPs

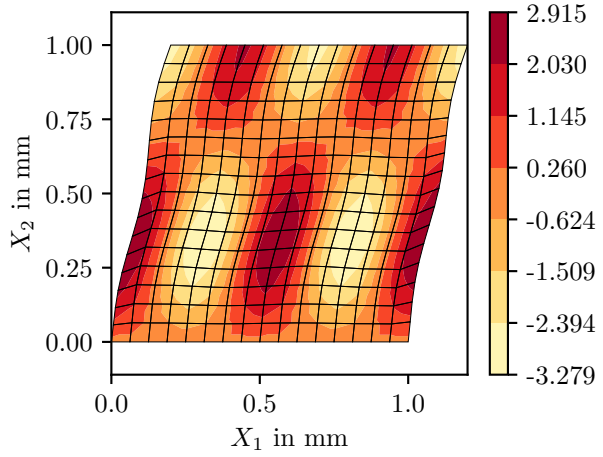

(c) 4x4 in 16x16 fully integrated 32x32 IPs

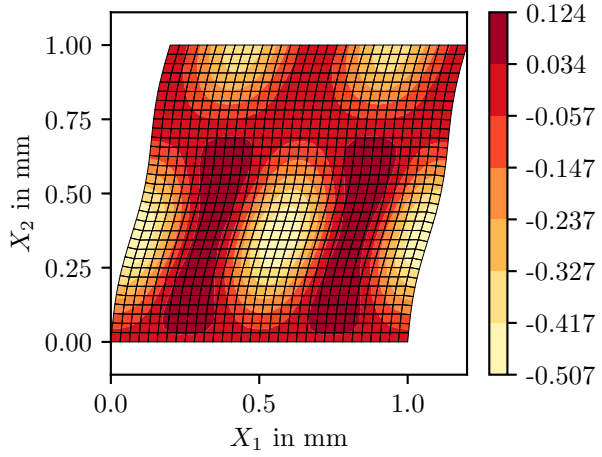

(d) 4x4 in 32x32 reduced integrated 32x32 IPs

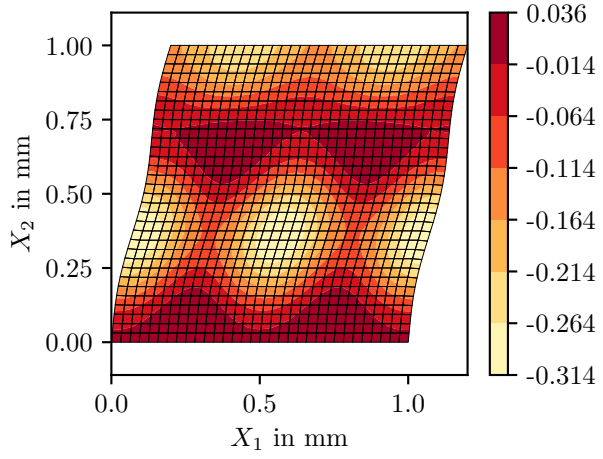

(e) 4x4 in 32x32 fully integrated 64x64 IPs

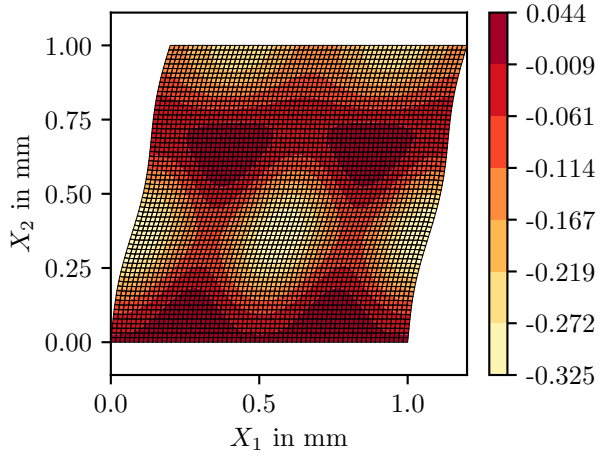

(f) 4x4 in 64x64 reduced integrated 64x64 IPs

Figure 9: Rotation fields of the continuum model with D_{55}^{neg} and D_{66}^{neg} using full and reduced integration for various discretization MxM representing a 4x4 discrete lattice.

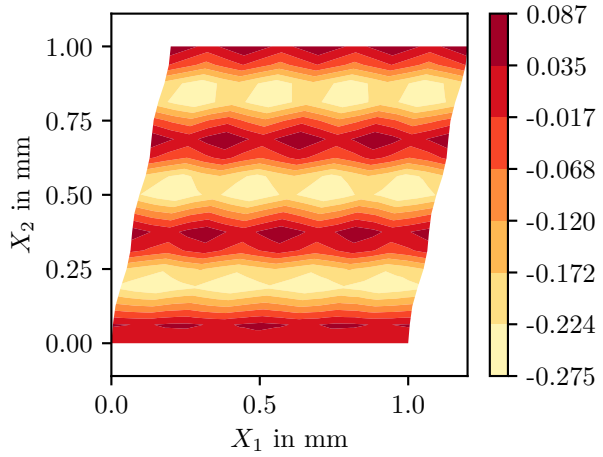

(a) 8x8 in 16x16

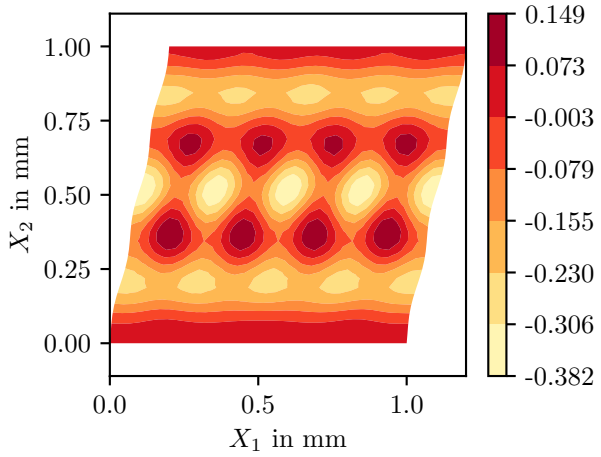

(b) 8x8 in 32x32

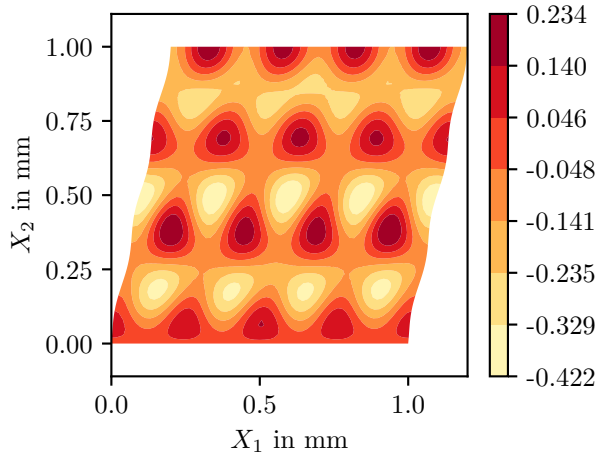

(c) 8x8 in 64x64

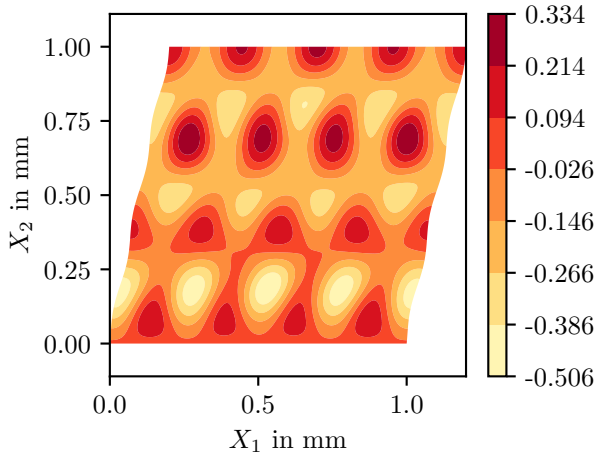

(d) 8x8 in 128x128

Figure 10: Rotation fields of the continuum model with D_{55}^{neg} and D_{66}^{neg} for various discretization MxM representing a 8x8 discrete lattice.

4.2.2 Lattice Beam under Bending

Lattice beams comprising 50x5 and 100x10 base cells are subjected to bending and are studied as more realistic engineering problems, cf. Figure 3. Their dimensions and material properties are listed in Table 5. The volume fraction of the parent material to the overall domain is kept constant, namely, resulting in 9.75%, with respect to all models. *Closed-* and *open-boundary* discrete lattice models, constructed by planar, linear TIMOSHENKO beam elements, serve as references for comparison with the continuum models discretized by `CPE4MP` elements.

Table 5: Geometrical dimensions and material constants regarding the bending load case.

	L_1 in mm	L_2 in mm	E_s in MPa	ν_s (/)	l_1 in mm	l_2 in mm	t in mm	NxN (/)
Bending I	200.0	20.0	120000.0	0.3	4.0	4.0	0.2	50x5
Bending II	200.0	20.0	120000.0	0.3	2.0	2.0	0.1	100x10

Strain energy

The strain energies of *closed-* and *open-boundary* discrete lattice models comprising 50x5 and 100x10 base cells are compared to the corresponding continuum counterparts considering positive and negative material constants for different mesh refinements MxM, cf. Figure 11. The strain energy of the continuum model shows the same convergence behavior, which depends on the sign of the material constants D_{55} and D_{66}, as has already been observed for the shear load case. The strain energies of the continuum model with positive material constants are in good agreement with the corresponding discrete models, where the strain energies of the latter represent the lower and upper bound. In contrast to the shear load case, the strain energies for all levels of discretization MxM are within these bounds for positive material constants. This is not the case, if negative material constants are used in combination with element sizes below the characteristic length, l.

Furthermore, the strain energies of the discrete model comprising 50x5 base cells and the corresponding continuum counterparts with positive and negative material constants are directly compared in order to emphasize the influence of the material constants, see Figure 12. It clearly shows, if the element sizes are used below the characteristic length, l, in combination with negative constants, the structural response is too stiff compared to the other cases, i.e., the strain energy stored in the beams is overestimated.

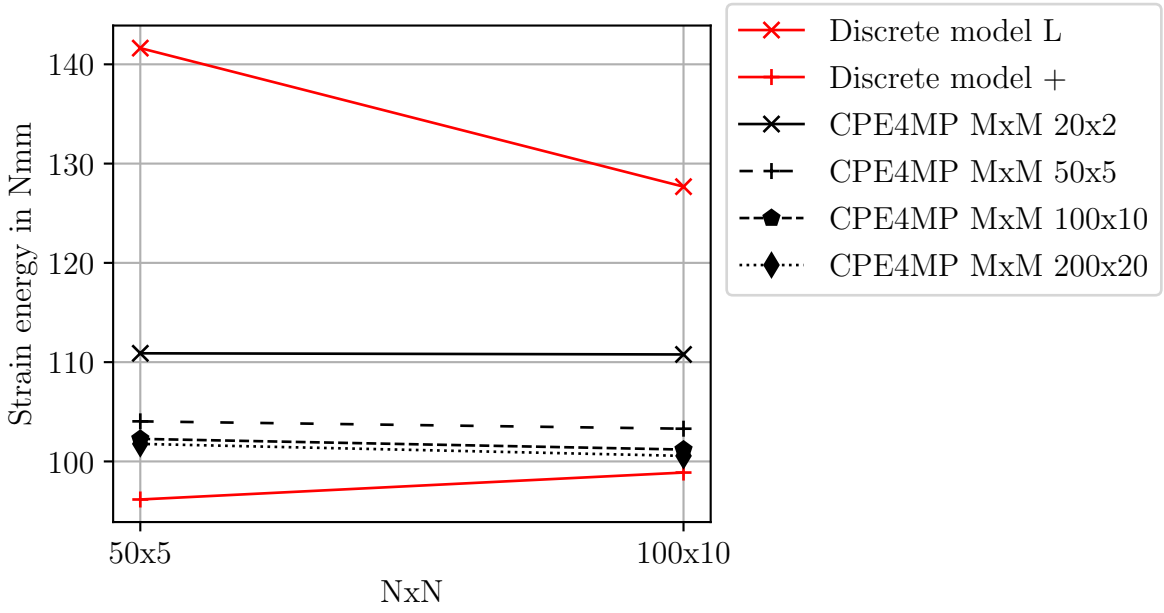

(a) D_{55}^{pos} and D_{66}^{pos}

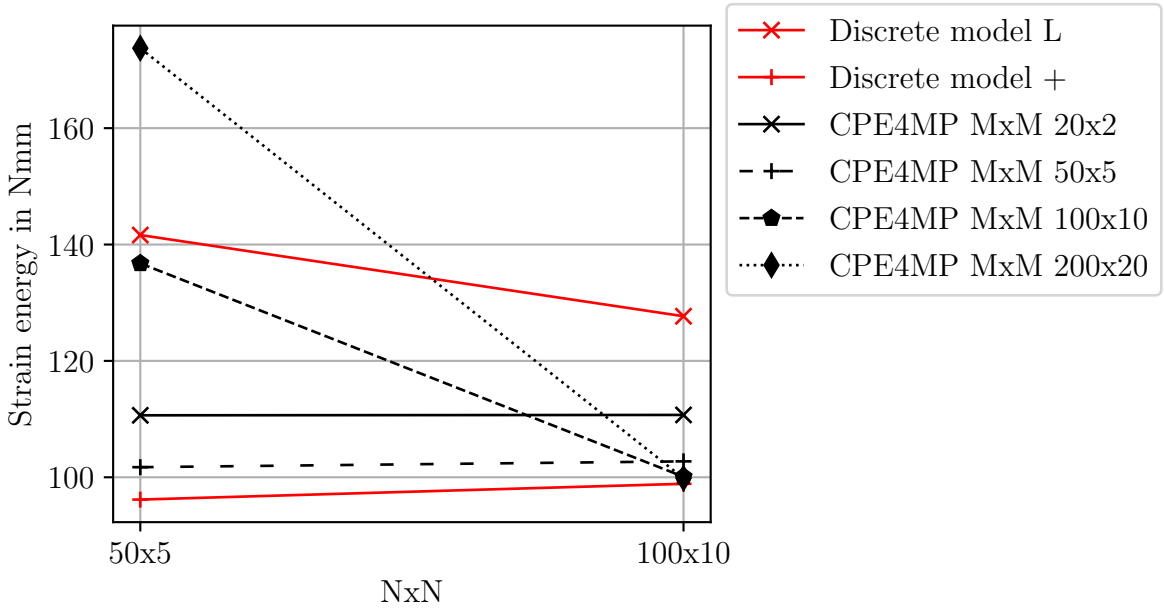

(b) D_{55}^{neg} and D_{66}^{neg}

Figure 11: Comparison of strain energies of *closed-* and *open-boundary* discrete lattice models comprising 50x5 and 100x10 base cells as well as corresponding continuum counterparts under mesh refinement MxM considering D_{55}^{pos} and D_{66}^{pos} as well as D_{55}^{neg} and D_{66}^{neg} for (a) and (b), respectively.

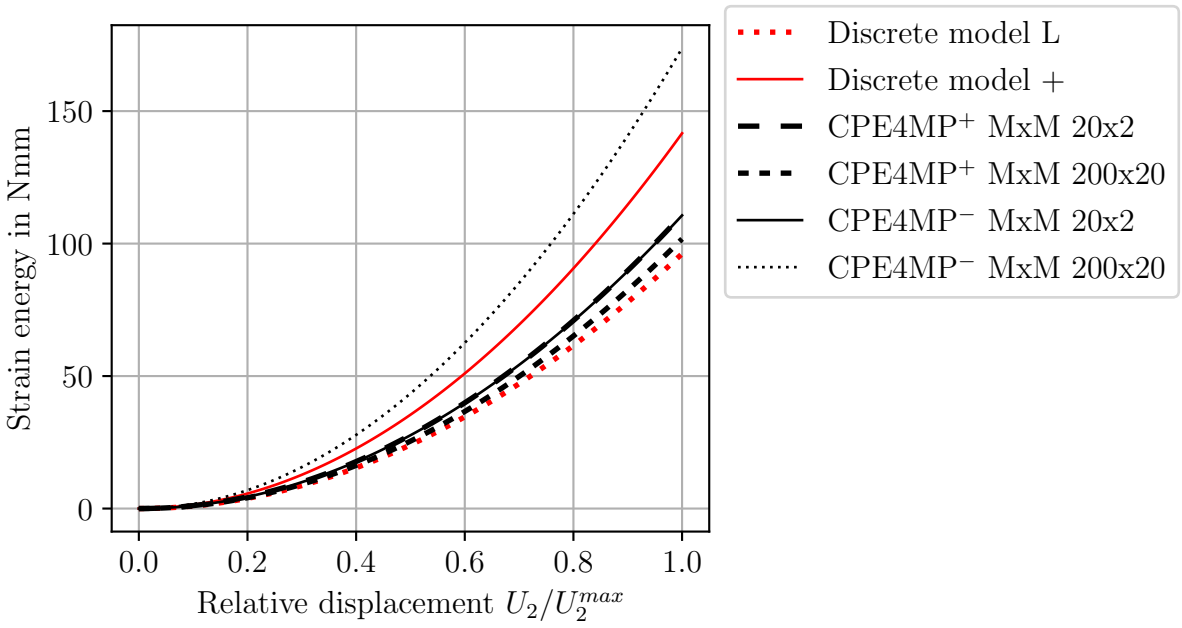

Figure 12: Comparison of strain energies of *closed-* and *open-boundary* discrete lattice models comprising 50x5 base cells as well as corresponding continuum counterparts considering D_{55}^{pos} and D_{66}^{pos} as well as D_{55}^{neg} and D_{66}^{neg} discretized by 20x2 and 200x20 elements.

Rotation field

All further investigations are based on the *open-boundary* lattice comprising 100x10 base cells. A direct comparison of the rotations between discrete and continuum model is given in Figure 13. The rotations are evaluated along the first element row below the neutral axis of the physical lattice at $x_2 = 9.0$. Nodal values are directly extracted for the discrete model. For the continuum model interpolated values are determined with respect to the physical intersection points of the lattice. The method has already been described in detail for the shear load case section, see Section 4.2.1. The domain of the continuum models is discretized by 20x2 and 100x10 elements in order to assess the behavior under mesh refinement.

The rotations of the continuum model with positive constants are in good agreement with the discrete model for both discretizations as given in Figures 13a and 13b. Using the coarse mesh results in a small offset in the rotations between discrete and continuum model along the entire 1-direction. The high gradient of the rotations at the intersection points can be captured quite well by the continuum model using positive material constants and a mesh size smaller than the characteristic length l. But as already discussed in Section 4.2.1, the continuum model is not capable of capturing local gradients in the rotation field.

The rotations of the continuum model with negative constants is only in agreement with the discrete model, when the element size is larger than the characteristic length as given in Figure 13c and 13d. For smaller element sizes the rotations show an oscillating behavior as has already been discussed in Section 4.2.1. It is worth noting, that the rotations at every second intersection point is in good agreement with the discrete ones, see Figure 13d.

Additionally, the rotations at the intersection points of the physical lattice along the rows at $x_2 = [11.0, 13.0, 17.0, 19.0]$ are compared for discrete and continuum model with positive material constants in Figure 14. Thereby, a discretization of 100x10 continuum elements is used. The continuum model captures the rotations fairly well when compared to the discrete reference, except for the case, when coming closer to the free surface of the lattice

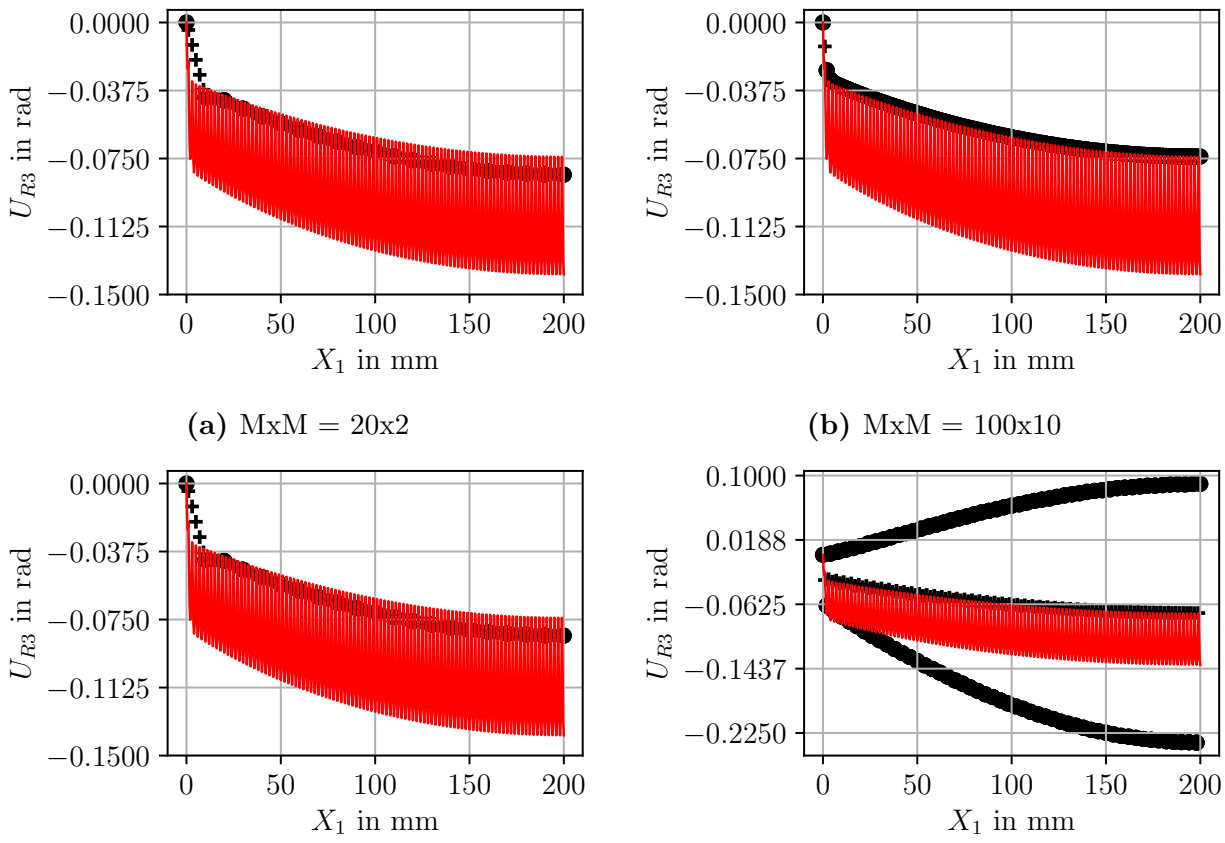

(a) MxM = 20x2 **(b)** MxM = 100x10

(c) MxM = 20x2 **(d)** MxM = 100x10

Figure 13: Nodal rotation U_{R3} of discrete lattice along neutral axis at $x_2 = 9.0$ indicated by the solid line and of continuum model with positive and negative material constants for (a) & (b) and (c) & (d), respectively, indicated by the markers. The markers + and • correspond to intersection nodes of the lattice at $x_2 = 9.0$ and to nodes at $x_2 = 9.0 + l_1/2$, respectively.

at $x_1 = 19.0$. This is to be expected since free edge effects cannot be correctly captured in continuum modeling.

The displacements in 1-direction, U_1, and rotations, U_{R3}, at the most east column of the lattice at $x_1 = 199.0$ are depicted in Figure 15 for the discrete and continuum model, respectively. The continuum model with positive constants captures the S-shaped macroscopic shear deformation fairly well as indicated by U_1. This also applies to the use of negative constants as the element size is below the characteristic length, l. The rotations show the same behavior as already observed for the simple shear load case, namely, that the use of

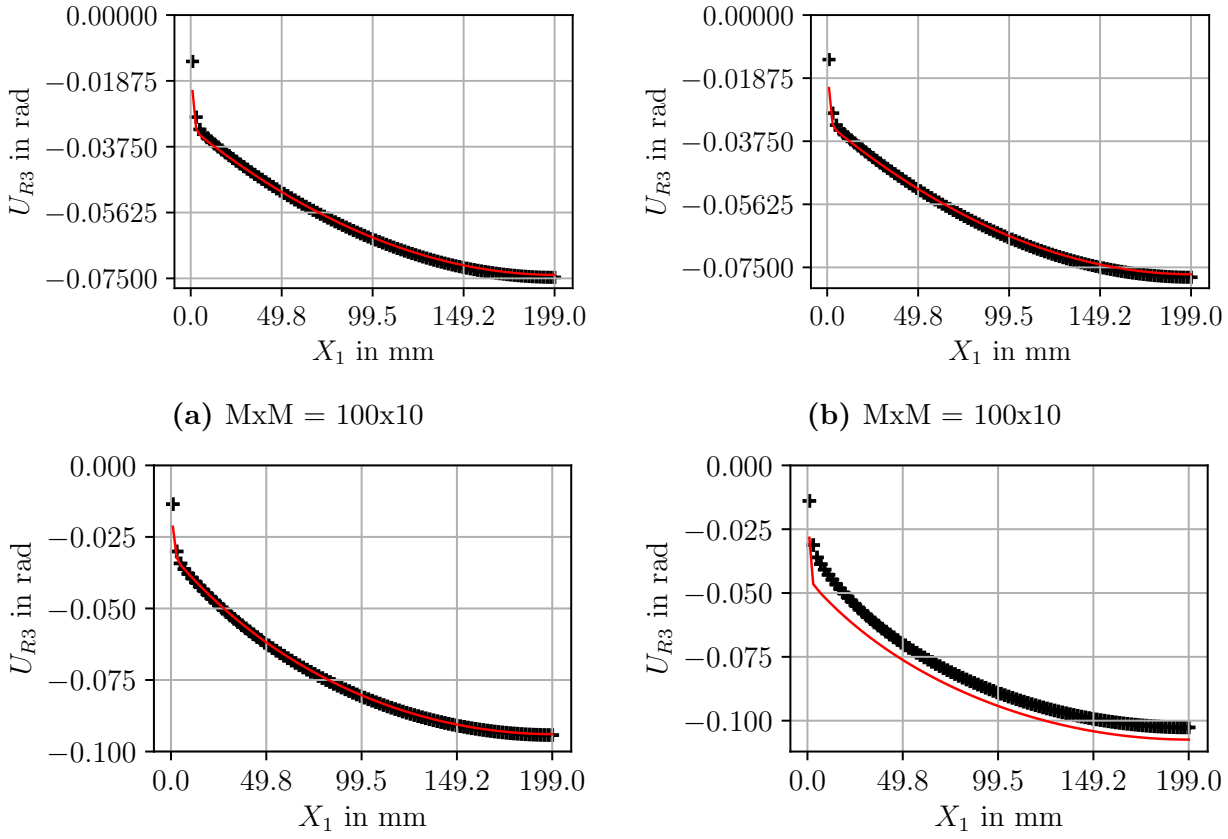

(a) MxM = 100x10

(b) MxM = 100x10

(c) MxM = 100x10

(d) MxM = 100x10

Figure 14: Rotation U_{R3} of intersection nodes along rows of lattice at fixed positions $x_2 = [11.0, 13.0, 17.0, 19.0]$ of discrete model indicated by the solid line and continuum counterpart (MxM = 100x10) with positive material constants for (a)-(d), respectively, indicated by the + markers.

negative material constants leads to oscillatory behavior under mesh refinement. This is not explicitly depicted in the current report, but is already indicated by the offset between the markers + and • in Figure 15d. In the current case the continuum element size is equal to the lattice size and already represents the limit case for negative material constants. In contrast, the rotations are captured well if positive material constants are used.

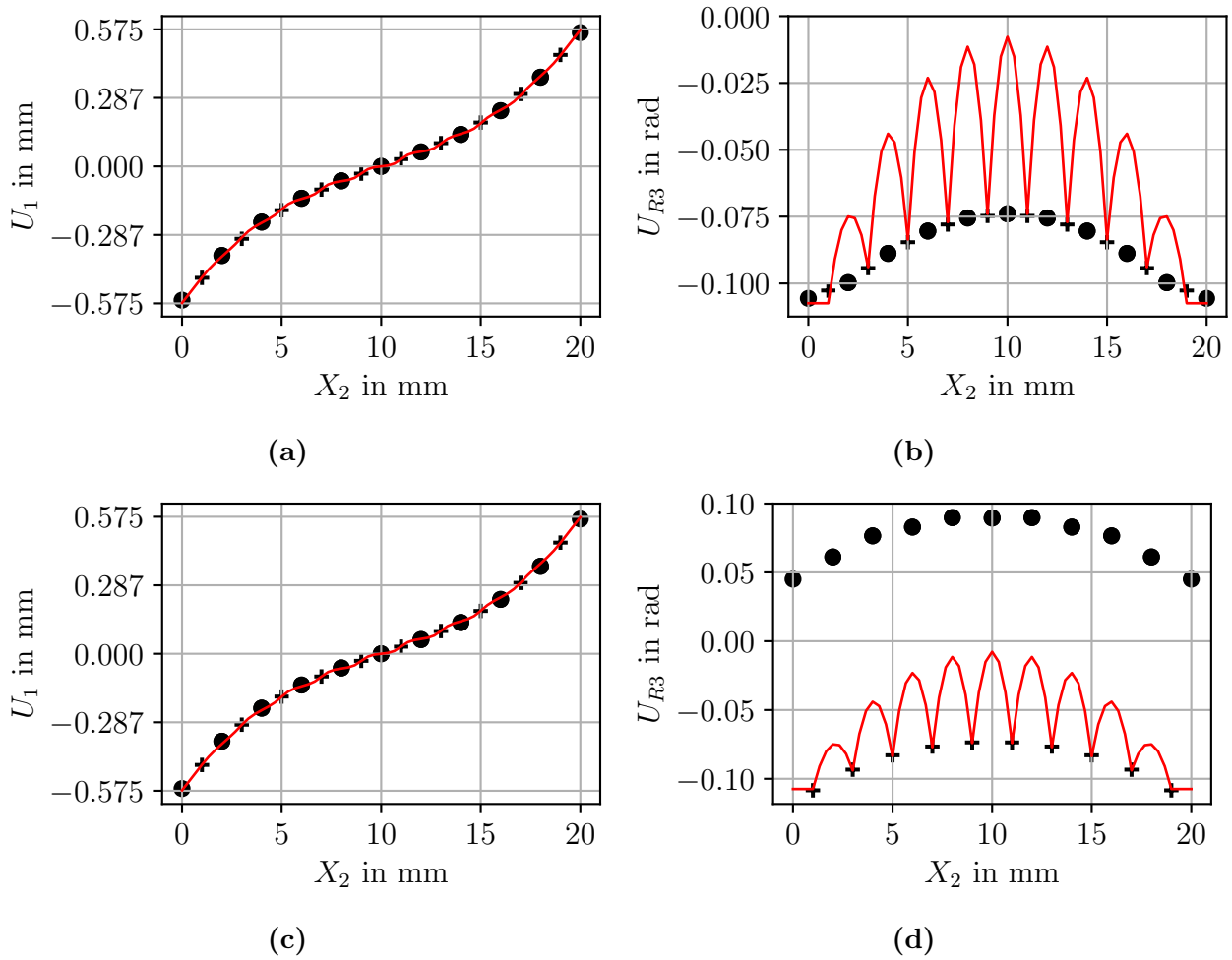

Figure 15: Nodal displacement U_1 and rotation U_{R3} of discrete lattice along the column at $x_1 = 199.0$ indicated by the solid line and of continuum counterpart with positive and negative material constants for (a) & (b) and (c) & (d), respectively, indicated by the markers. The markers + and • correspond to intersection nodes of the lattice at $x_1 = 199.0$ and to nodes at $x_1 = 199.0 + l_1/2$, respectively.

5 Conclusion and Outlook

A micropolar continuum plain strain user element is implemented within the framework of the commercial FEM-solver `ABAQUS` based on [15]. Micropolar field theory is exploited to account for the mechanical response of square lattices restricted to the linear regime. A patch-test is performed to ensure correct implementation. For investigating the predictive capabilities of the element with respect to the structural response, a simple shear and a bending load case are conducted, where discrete models served as reference.

The rotations at the intersection points of the lattice for discrete and continuum model show very good agreement in the far-field of the bearing point when using positive material constants related to the microcurvature for both load cases. This is also true for negative material constants, expect when the element size is below or equal to the characteristic length, l, of the lattice. High gradients in the rotation field near the clamped edge could only be resolved when the element sizes are below the characteristic length, l, in combination with positive material constants. The authors in [15] note that especially the requirement of the element size being greater than the characteristic cell size limits the application of the proposed model in the area of large gradients of stresses and strains. This requirement is to the best of the author's experience only true, when negative micropolar constants are used. Thus, there seems to be no restriction on the element size when using positive constants, which is an important finding of the current report.

The continuum model is not capable of capturing local fluctuations in the rotation field as provided by the discrete model. Higher order field theory, i.e., micromorphic continuum theory, in conjunction with an appropriate derivation of material constants may be necessary to account for these local rotation gradients.

The next step to advance the user element for capturing local structural instabilities, both, large displacements and strains have to be considered. Non-linear micropolar finite element

formulations considering large displacements and small strains have been presented, e.g., in [5] and [12]. How to deal with finite strains and curvatures has been presented in, e.g., [6], [18] and [23] accounting for hyper-elastic and hypo-elastic materials, respectively. In the case of continuum modeling of lattice structures, finite strains are governed by large displacements of the underlying microstructure rather than by material nonlinearities of the parent material. Therefore, an asymptotic homogenization approach considering lattice structures, as proposed by [11], might be a reasonable choice.

A Appendix

The shape functions for the quadrilateral element (e) in natural space are given as

$$N_1^{(e)} = \frac{1}{4}(1-\xi)(1-\eta) \qquad N_2^{(e)} = \frac{1}{4}(1+\xi)(1-\eta)$$
$$N_3^{(e)} = \frac{1}{4}(1+\xi)(1+\eta) \qquad N_4^{(e)} = \frac{1}{4}(1-\xi)(1+\eta).$$

Geometry, displacement and rotation fields are approximated by

$$x_1 \approx \sum_{i=1}^{N=4} N_i^{(e)} \cdot X_{1\#i}^{(e)} \qquad x_2 \approx \sum_{i=1}^{N=4} N_i^{(e)} \cdot X_{2\#i}^{(e)}$$
$$u_1 \approx \sum_{i=1}^{N=4} N_i^{(e)} \cdot U_{1\#i}^{(e)} \qquad u_2 \approx \sum_{i=1}^{N=4} N_i^{(e)} \cdot U_{2\#i}^{(e)}$$
$$\phi \approx \sum_{i=1}^{N=4} N_i^{(e)} \cdot \phi_{\#i}^{(e)} \quad ,$$

where $X_{1\#i}$, $X_{2\#i}$, $U_{1\#i}$, $U_{2\#i}$, and $\phi_{\#i}$ are the coordinates in 1- and 2-direction, the displacements in 1- and 2-direction, and the rotation of node i for the element (e).

The nodal displacements and rotation are stored in the displacement-rotation-vector of an element (e) in the form

$$[\underline{\mathbf{U}}^{(e)}] = [U_{1\#1}^{(e)}, U_{2\#1}^{(e)}, \phi_{\#1}^{(e)}, \ldots, U_{1\#4}^{(e)}, U_{2\#4}^{(e)}, \phi_{\#4}^{(e)}]^{\mathrm{T}}.$$

The resulting shape functions matrix can then be given as

$$[\underset{\sim}{\mathbf{N}}^{(e)}] = \begin{bmatrix} N_1 & 0 & 0 & N_2 & 0 & 0 & N_3 & 0 & 0 & N_4 & 0 & 0 \\ 0 & N_1 & 0 & 0 & N_2 & 0 & 0 & N_3 & 0 & 0 & N_4 & 0 \\ 0 & 0 & N_1 & 0 & 0 & N_2 & 0 & 0 & N_3 & 0 & 0 & N_4 \end{bmatrix}. \tag{15}$$

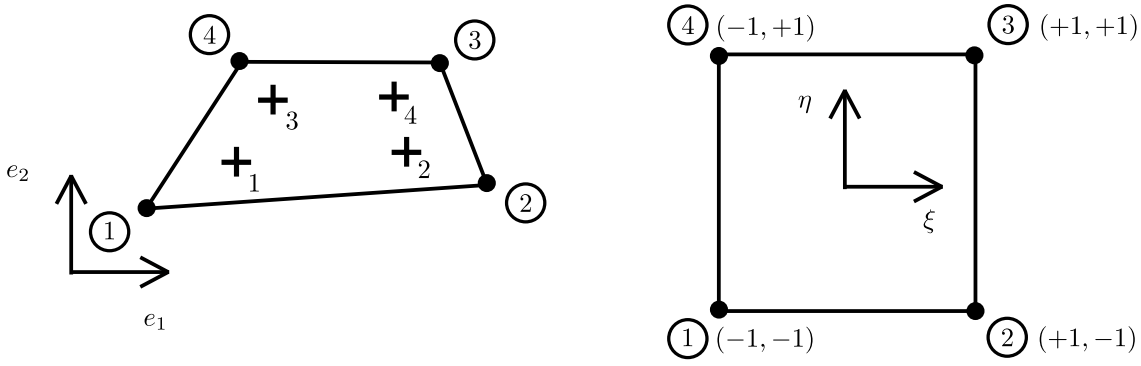

Figure 16: Linearly interpolated quadrilateral element with node and integration point numbering.

The differential operator matrix follows from the linearized vector of strain components as given in Eq. 8 as

$$[\underset{\sim}{\mathbf{d}}] = \begin{bmatrix} \dfrac{\partial}{\partial x_1} & 0 & 0 \\ 0 & \dfrac{\partial}{\partial x_2} & 0 \\ 0 & \dfrac{\partial}{\partial x_1} & -1 \\ \dfrac{\partial}{\partial x_2} & 0 & 1 \\ 0 & 0 & \dfrac{\partial}{\partial x_1} \\ 0 & 0 & \dfrac{\partial}{\partial x_2} \end{bmatrix},$$

with $\underline{\varepsilon} = [\underset{\sim}{\mathbf{d}}]\vec{u}$. Thereby, $\vec{u}$ denotes the physical continuous displacement/rotation field $\vec{u} = [u_1, u_2, \phi]^{\mathrm{T}}$.

The shape functions derivative matrix then results in

$$[\underset{\sim}{\mathbf{B}}_{\mathrm{N}}^{(e)}] = [\underset{\sim}{\mathbf{d}}][\underset{\sim}{\mathbf{N}}^{(e)}] = \begin{bmatrix} \frac{\partial N_1}{\partial x_1} & 0 & 0 & \frac{\partial N_2}{\partial x_1} & 0 & 0 & \frac{\partial N_3}{\partial x_1} & 0 & 0 & \frac{\partial N_4}{\partial x_1} & 0 & 0 \\ 0 & \frac{\partial N_1}{\partial x_2} & 0 & 0 & \frac{\partial N_2}{\partial x_2} & 0 & 0 & \frac{\partial N_3}{\partial x_2} & 0 & 0 & \frac{\partial N_4}{\partial x_2} & 0 \\ 0 & \frac{\partial N_1}{\partial x_1} & -N_1 & 0 & \frac{\partial N_2}{\partial x_1} & -N_2 & 0 & \frac{\partial N_3}{\partial x_1} & -N_3 & 0 & \frac{\partial N_4}{\partial x_1} & -N_4 \\ \frac{\partial N_1}{\partial x_2} & 0 & N_1 & \frac{\partial N_2}{\partial x_2} & 0 & N_2 & \frac{\partial N_3}{\partial x_2} & 0 & N_3 & \frac{\partial N_4}{\partial x_2} & 0 & N_4 \\ 0 & 0 & \frac{\partial N_1}{\partial x_1} & 0 & 0 & \frac{\partial N_2}{\partial x_1} & 0 & 0 & \frac{\partial N_3}{\partial x_1} & 0 & 0 & \frac{\partial N_4}{\partial x_1} \\ 0 & 0 & \frac{\partial N_1}{\partial x_2} & 0 & 0 & \frac{\partial N_2}{\partial x_2} & 0 & 0 & \frac{\partial N_3}{\partial x_2} & 0 & 0 & \frac{\partial N_4}{\partial x_2} \end{bmatrix}$$

where the derivatives of the shape functions are given with respect to spatial coordinates x_1 and x_2

$$\frac{\partial N_i}{\partial x_1} = \frac{\partial N_i}{\partial \xi} J_{11}^{-1} + \frac{\partial N_i}{\partial \eta} J_{12}^{-1}$$

$$\frac{\partial N_i}{\partial x_2} = \frac{\partial N_i}{\partial \xi} J_{21}^{-1} + \frac{\partial N_i}{\partial \eta} J_{22}^{-1}$$

with J_{ij}^{-1} as the components of the inverse Jacobian matrix. The Jacobian is defined as

$$\begin{bmatrix} \frac{\partial}{\partial \xi} \\ \frac{\partial}{\partial \eta} \end{bmatrix} = \underbrace{\begin{bmatrix} \frac{\partial x_1}{\partial \xi} & \frac{\partial x_2}{\partial \xi} \\ \frac{\partial x_1}{\partial \eta} & \frac{\partial x_2}{\partial \eta} \end{bmatrix}}_{\left[\underset{\sim}{\mathbf{J}}^{(e)}\right]} \begin{bmatrix} \frac{\partial}{\partial x_1} \\ \frac{\partial}{\partial x_2} \end{bmatrix}$$

with

$$J_{11}^{(e)} = \frac{\partial N_i^{(e)}}{\partial \xi} X_{1\#i}^{(e)}, \quad J_{12}^{(e)} = \frac{\partial N_i^{(e)}}{\partial \xi} X_{2\#i}^{(e)}, \quad J_{21}^{(e)} = \frac{\partial N_i^{(e)}}{\partial \eta} X_{1\#i}^{(e)}, \quad J_{22}^{(e)} = \frac{\partial N_i^{(e)}}{\partial \eta} X_{2\#i}^{(e)}$$

The element stiffness matrix, $[\underset{\sim}{\mathbf{K}}^{(e)}]$, is determined by using a full or reduced Gaussian quadrature scheme, cf. Table 6. All quantities are evaluated at the integration points coordinates ξ_i, η_i, where i describes the integration point number, see Table 6.

$$\begin{aligned}
[\underset{\sim}{\mathbf{K}}^{(e)}] &= \int_{Vol} [\underset{\sim}{\mathbf{B}}_{\mathrm{N}}^{(e)}]^{\mathrm{T}} [\underset{\sim}{\mathbb{D}}] [\underset{\sim}{\mathbf{B}}_{\mathrm{N}}^{(e)}] \mathrm{d}Vol \\
&= \int_{-1}^{+1} \int_{-1}^{+1} [\underset{\sim}{\mathbf{B}}_{\mathrm{N}}^{(e)}]^{\mathrm{T}}(\xi,\eta) [\underset{\sim}{\mathbb{D}}] [\underset{\sim}{\mathbf{B}}_{\mathrm{N}}^{(e)}](\xi,\eta) h(\xi,\eta) \mathrm{d}\xi \mathrm{d}\eta \\
&\approx \sum_{i=1}^{n_{int}} [\underset{\sim}{\mathbf{B}}_{\mathrm{N}}^{(e)}]^{\mathrm{T}}(\xi_i,\eta_i) [\underset{\sim}{\mathbb{D}}] [\underset{\sim}{\mathbf{B}}_{\mathrm{N}}^{(e)}](\xi_i,\eta_i) \det[\underset{\sim}{\mathbf{J}}^{(e)}](\xi_i,\eta_i) h(\xi_i,\eta_i) w_i
\end{aligned}$$

The right hand-side force vector (or internal force vector) as a requested quantity by the `ABAQUS` FEM solver is computed as

$$\begin{aligned}
\underline{\mathbf{F}}_{int} &= \int_{Vol} [\underset{\sim}{\mathbf{B}}_{\mathrm{N}}^{(e)}]^{\mathrm{T}} [\underline{\boldsymbol{\sigma}}] \mathrm{d}Vol \\
&= \int_{-1}^{+1} \int_{-1}^{+1} [\underset{\sim}{\mathbf{B}}_{\mathrm{N}}^{(e)}]^{\mathrm{T}}(\xi,\eta) [\underline{\boldsymbol{\sigma}}](\xi,\eta) h(\xi,\eta) \mathrm{d}\xi \mathrm{d}\eta \\
&\approx \sum_{i=1}^{n_{int}} [\underset{\sim}{\mathbf{B}}_{\mathrm{N}}^{(e)}]^{\mathrm{T}}(\xi_i,\eta_i) [\underline{\boldsymbol{\sigma}}](\xi_i,\eta_i) \det([\underset{\sim}{\mathbf{J}}^{(e)}](\xi_i,\eta_i)) w_i
\end{aligned}$$

Table 6: Gaussian integration point coordinates and corresponding weights.

Full integration with number of integration points $n_{int} = 4$.

i	ξ_i	η_i	w_i
1	$-\frac{1}{\sqrt{3}}$	$-\frac{1}{\sqrt{3}}$	1.0
2	$+\frac{1}{\sqrt{3}}$	$-\frac{1}{\sqrt{3}}$	1.0
3	$+\frac{1}{\sqrt{3}}$	$+\frac{1}{\sqrt{3}}$	1.0
4	$-\frac{1}{\sqrt{3}}$	$+\frac{1}{\sqrt{3}}$	1.0

Reduced integration with number of integration points $n_{int} = 1$.

i	ξ_i	η_i	w_i
1	0	0	4.0

B Appendix

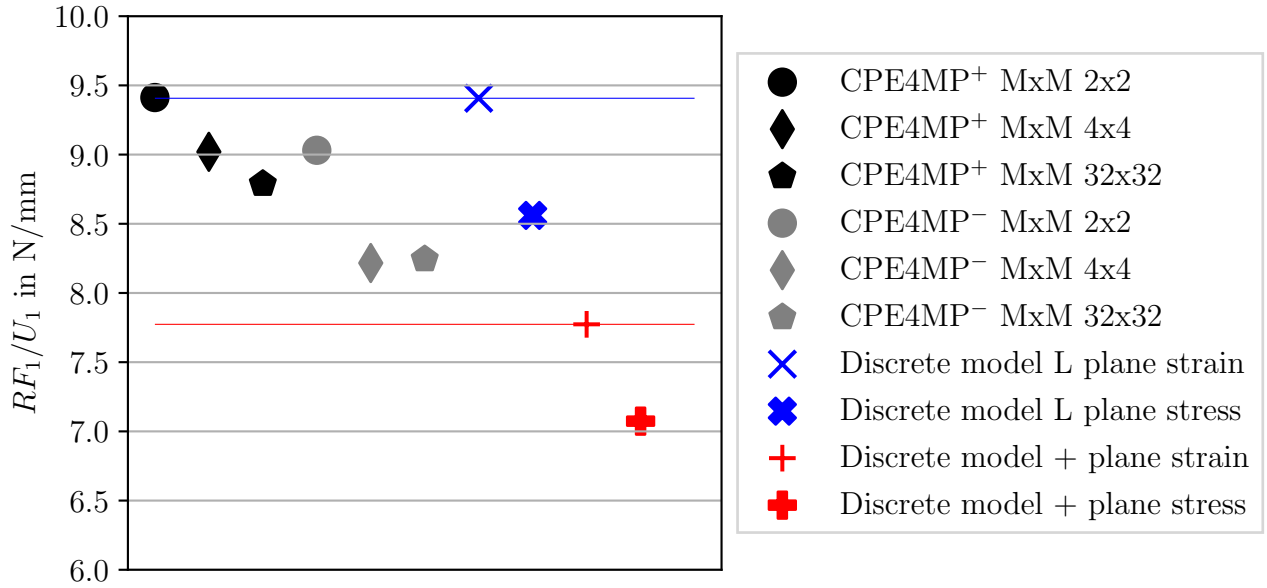

(a) NxN = 4x4

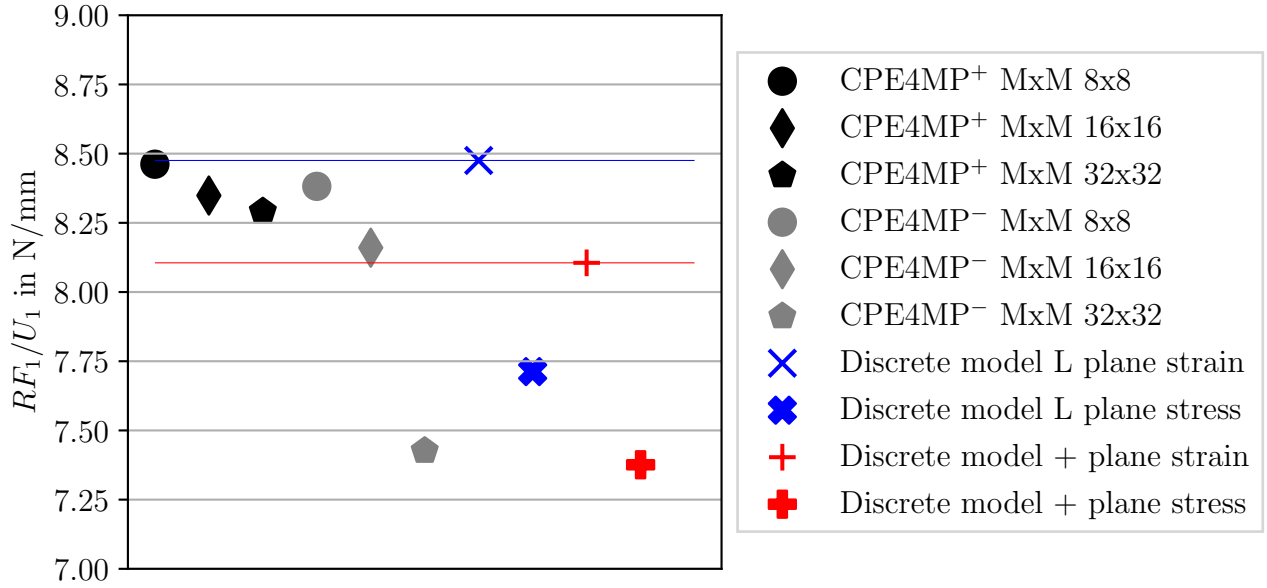

(b) NxN = 16x16

Figure 17: Reaction force per displacement of discrete and continuum models describing a 4x4 and 16x16 square lattice for (a) and (b), respectively.

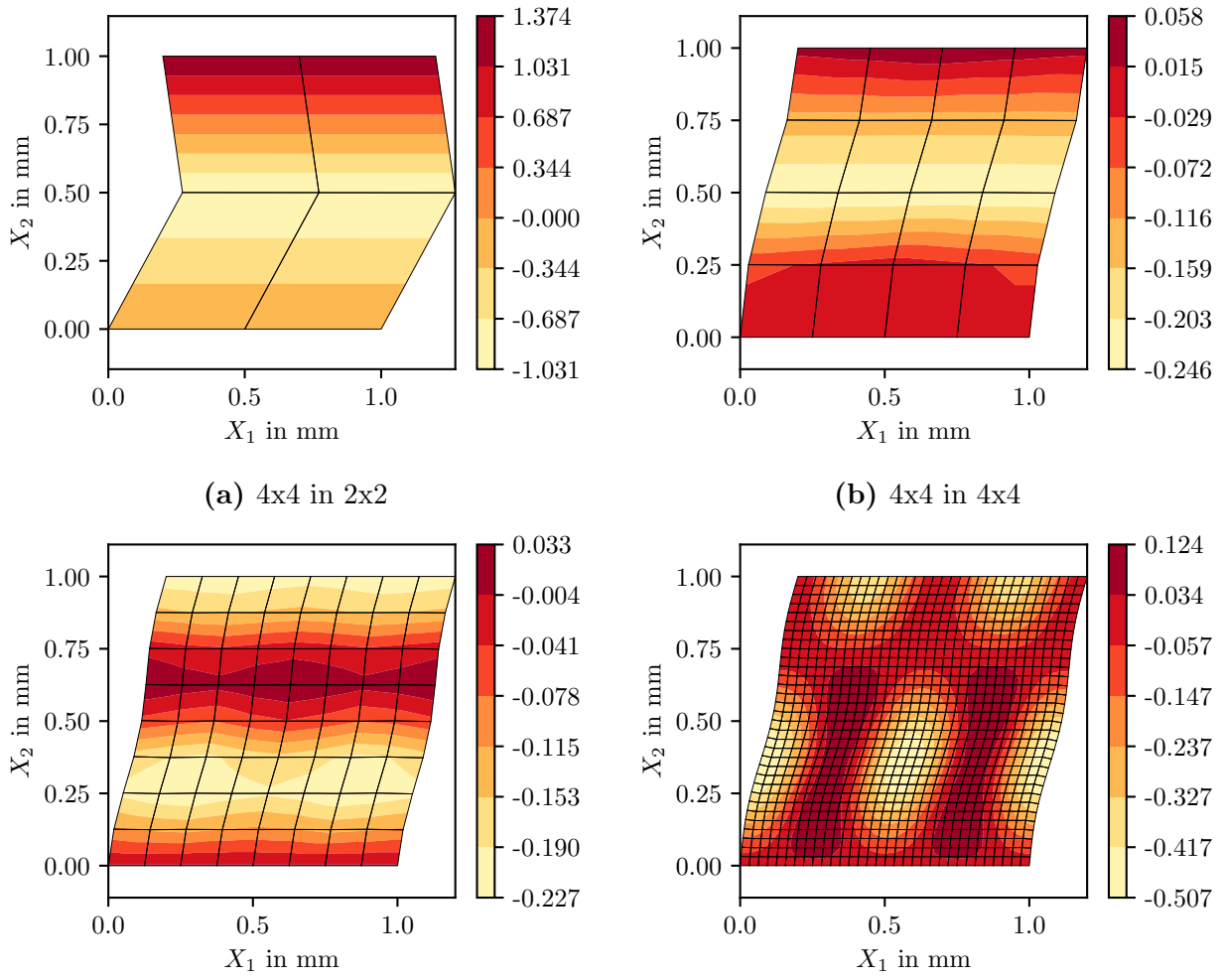

(a) 4x4 in 2x2

(b) 4x4 in 4x4

(c) 4x4 in 8x8

(d) 4x4 in 32x32

Figure 18: Rotation fields of the continuum model with D_{55}^{neg} and D_{66}^{neg} using reduced integration for various discretizations MxM representing a 4x4 discrete lattice.

C Appendix

A slight inconsistency could be noticed within the equations for *Test 2* and *Test 3* in [22] (see Table 3 therein) regarding the value of the constant α. The value of α is not given explicitly in [22] and, therefore, is chosen as $\alpha = 0.5$ in order to obtain the given couple stress values $m_1 = -m_2 = 0.04$ for *Test 3* when considering the given material constant $l = 0.1$. Consequently, *Test 2* considering $\alpha = 0.5$ results in stress values of $\sigma_{12} = 1.375$ and $\sigma_{21} = 1.625$, contradicting the values $\sigma_{12} = 1$ and $\sigma_{21} = 2$ as given in [22]. The latter will only be obtained either choosing $\alpha = 2$ or changing the arrangement of parentheses in the equations from $(1/4\alpha)$ to $1/(4\alpha)$. The rearrangement of parentheses is confirmed by the equations given for σ_{12} and σ_{21} for *Test 3*. These values can only be preserved when choosing $\alpha(= a) = 0.5$, where α is the material constant given in Table 2, and rearranging the parenthesis in the equation of ϕ from $(1/2\alpha)$ to $1/(2\alpha)$. A direct comparison of the equations is given below, where the equations on the left and right hand-side correspond to the given ones in [22] and the ones used in the current report, respectively.

$$\begin{aligned} &\textit{Test 2}: && \phi = 10^{-3}((1/4) + (1/4\alpha)) \Rightarrow \phi = 10^{-3}((1/4) + 1/(4\alpha)) \\ &\textit{Test 3}: && \phi = 10^{-3}((1/4) + (1/2\alpha)(x_1 - x_2)) \Rightarrow 10^{-3}((1/4) + 1/(2\alpha)(x_1 - x_2)) \end{aligned} \tag{16}$$

References

[1] ABAQUS/Standard User's Manual Version 2019. Dassault Systemes Simulia. Providence, RI, USA.

[2] H. Altenbach and V. A. Eremeyev. Cosserat Media. *CISM International Centre for Mechanical Sciences, Courses and Lectures*, 541:65–130, 2013.

[3] M. F. Ashby and L. Gibson. *Cellular Solids, Structures and Properties*. Pergamon Press, 1988.

[4] K. J. Bathe. *Finite Element Procedures*. K.J. Bathe, Watertown, MA, 2nd edition, 2014.

[5] S. Bauer, M. Schäfer, P. Grammenoudis, and C. Tsakmakis. Three-dimensional finite elements for large deformation micropolar elasticity. *Computer Methods in Applied Mechanics and Engineering*, 199(41-44):2643–2654, 2010.

[6] S. Bauer, W. G. Dettmer, D. Perić, and M. Schäfer. Micropolar hyperelasticity: Constitutive model, consistent linearization and simulation of 3D scale effects. *Computational Mechanics*, 50(4):383–396, 2012.

[7] Z. P. Bažant and M. Christensen. Analogy between micropolar continuum and grid frameworks under initial stress. *International Journal of Solids and Structures*, 8(3): 327–346, 1972.

[8] F. Cosserat and E. Cosserat. *Théorie des corps déformables*. Hermann et fils, 1909.

[9] F. Dell'Isola, I. Giorgio, M. Pawlikowski, and N. L. Rizzi. Large deformations of planar extensible beams and pantographic lattices: heuristic homogenization, experimental and numerical examples of equilibrium. *Proceedings of the Royal Society A: Mathematical, Physical and Engineering Sciences*, 472(2185):20150790, 2016.

[10] A. Desmoulins and D. Kochmann. Local and nonlocal continuum modeling of inelastic periodic networks applied to stretching-dominated trusses. *Computer Methods in Applied Mechanics and Engineering*, 313:85–105, 2017.

[11] K. ElNady, I. Goda, and J. F. Ganghoffer. Computation of the effective nonlinear mechanical response of lattice materials considering geometrical nonlinearities. *Computational Mechanics*, 58(6):957–979, 2016.

[12] S. G. Erdelj, G. Jelenić, and A. Ibrahimbegović. Geometrically non-linear 3D finite-element analysis of micropolar continuum. *International Journal of Solids and Structures*, 202:745–764, 2020.

[13] A. C. Eringen. *Microcontinuum Field Theories*. Springer-Verlag New York, Inc., 1999.

[14] B. M. Irons and A. Razzaque. Experience with the patch test for convergence of finite elements. In A. K. Aziz, editor, *The Mathematical Foundations of the Finite Element Method with Applications to Partial Differential Equations*, pages 557–587. Academic Press, 1972.

[15] R. S. Kumar and D. L. McDowell. Generalized continuum modeling of 2-D periodic cellular solids. *International Journal of Solids and Structures*, 41(26):7399–7422, 2004.

[16] M. H. Luxner, J. Stampfl, and H. E. Pettermann. Numerical simulations of 3D open cell structures - influence of structural irregularities on elasto-plasticity and deformation localization. *International Journal of Solids and Structures*, 44(9):2990–3003, 2007.

[17] P. Moongkhamklang, D. M. Elzey, and H. N. Wadley. Titanium matrix composite lattice structures. *Composites Part A: Applied Science and Manufacturing*, 39:176–187, 2008.

[18] I. Münch. *Ein geometrisch und materiell nichtlineares Cosserat-Modell - Theorie, Numerik und Anwendungsmöglichkeiten*. PhD thesis, Universität Karlsruhe (TH), 2007.

[19] A. K. Noor. Continuum modeling for repetitive lattice structures. *Applied Mechanics Reviews*, 41(7):285–297, 1988.

[20] R. K. Pal, M. Ruzzene, and J. J. Rimoli. A continuum model for nonlinear lattices under large deformations. *International Journal of Solids and Structures*, 96:300–319, 2016.

[21] G. P. Phlipot and D. M. Kochmann. A quasicontinuum theory for the nonlinear mechanical response of general periodic truss lattices. *Journal of the Mechanics and Physics of Solids*, 124:758–780, 2019.

[22] E. Providas and M. A. Kattis. Finite element method in plane Cosserat elasticity. *Computers and Structures*, 80(27-30):2059–2069, 2002.

[23] S. Ramezani, R. Naghdabadi, and S. Sohrabpour. Non-linear finite element implementation of micropolar hypo-elastic materials. *Computer Methods in Applied Mechanics and Engineering*, 197(49-50):4149–4159, 2008.

[24] P. Trovalusci and R. Masiani. Material symmetries of micropolar continua equivalent to lattices. *International Journal of Solids and Structures*, 36(14):2091–2108, 1999.

[25] M. Yoder, L. Thompson, and J. Summers. Size effects in lattice structures and a comparison to micropolar elasticity. *International Journal of Solids and Structures*, 143:245–261, 2018.